

1 **Thermomechanical response of thickly tamped targets and diamond anvil cells under**
2 **pulsed hard x-ray irradiation**

3 J. Meza-Galvez,^{1,2} N. Gomez-Perez,^{2,3,4} A. Marshall,² A.L. Coleman,^{2,5} K. Appel,⁶ H.P.
4 Liermann,⁷ M. I. McMahon,² Z. Konôpková,⁶ and R. S. McWilliams^{2, a)}

5 ¹⁾*Facultad de Química, Universidad Autónoma del Estado de México (UAEMéx),*
6 *Tollocan s/n, esq. Paseo Colón, Toluca, Estado de México, 50110,*
7 *México.*

8 ²⁾*The School of Physics and Astronomy, Centre for Science at Extreme Conditions,*
9 *and SUPA, University of Edinburgh, Peter Guthrie Tait Road, Edinburgh,*
10 *EH9 3FD, UK*

11 ³⁾*School of Mathematics, Statistics and Physics, Newcastle University,*
12 *Newcastle upon Tyne, NE1 7RU, UK*

13 ⁴⁾*British Geological Survey, Currie, EH14 4BA, UK*

14 ⁵⁾*Lawrence Livermore National Laboratory, 7000 East Avenue, Livermore,*
15 *CA 94550, USA*

16 ⁶⁾*European XFEL GmbH, Holzkoppel 4, 22869 Schenefeld,*
17 *Germany*

18 ⁷⁾*Deutsches Elektronen-Synchrotron (DESY) Photon Science, Notkestraße 85,*
19 *22607 Hamburg, Germany*

20 (Dated: 21 April 2020)

21 In the laboratory study of extreme conditions of temperature and density, the expo-
22 sure of matter to high intensity radiation sources has been of central importance. Here
23 we interrogate the performance of multi-layered targets in experiments involving high
24 intensity, hard x-ray irradiation, motivated by the advent of extremely high bright-
25 ness hard x-ray sources, such as free electron lasers and 4th-generation synchrotron
26 facilities. Intense hard x-ray beams can deliver significant energy in targets having
27 thick x-ray transparent layers (tamper) around samples of interest, for the study
28 of novel states of matter and materials' dynamics. Heated-state lifetimes in such
29 targets can approach the microsecond level, regardless of radiation pulse duration,
30 enabling the exploration of conditions of local thermal and thermodynamic equilib-
31 rium at extreme temperature in solid density matter. The thermal and mechanical
32 response of such thick layered targets following x-ray heating, including hydrody-
33 namic relaxation and heat flow on picosecond to millisecond timescales, is modeled
34 using radiation hydrocode simulation, finite element analysis, and thermodynamic
35 calculations. Assessing the potential for target survival over one or more exposures,
36 and resistance to damage arising from heating and resulting mechanical stresses, this
37 study doubles as an investigation into the performance of diamond-anvil high pres-
38 sure cells under high x-ray fluences. Long used in conjunction with synchrotron x-ray
39 radiation and high power optical lasers, the strong confinement afforded by such cells
40 suggests novel applications at emerging high intensity x-ray facilities and new routes
41 to studying thermodynamic equilibrium states of warm, very dense matter.

42 PACS numbers: 62.50.-p, 07.35.+k 52.59.Px 52.50.Jm 41.60.Cr

43 Keywords: diamond, anvil, cell, high, pressure, temperature, free, electron, laser,
44 heat, finite, element, numerical, model, hydrocode

^{a)}Electronic mail: rs.mcwilliams@ed.ac.uk

45 I. INTRODUCTION

46 Matter with an atomic density similar to that of the solid state, at temperatures of thou-
47 sands to millions of degrees Kelvin and pressures exceeding millions of atmospheres, and
48 undergoing rapid changes on microsecond to femtosecond timescales, is central to our un-
49 derstanding of planetary and stellar interiors, fusion energy technologies, and fundamental
50 materials physics and chemistry. These warm dense matter states are not well described
51 by the theoretical simplifications of traditional condensed matter physics or plasma physics.
52 Laboratory experiments are thus critical for developing a physical understanding of this
53 regime of temperature, density, pressure, and timescale. The creation and probing of warm
54 dense matter in the laboratory often relies on central facilities capable of delivering high-
55 brilliance irradiation, which can rapidly generate extreme temperatures in dense (i.e. solid
56 or liquid) targets by ultrafast (fs-ps) isochoric heating, or by the production of dynamic
57 compression waves within the target facilitated by the expansion of heated matter on longer
58 (ps-ns) timescales¹⁻³. Ultrafast techniques have been widely employed to study the case of
59 isochoric heating at timescales from femtosecond energy delivery to electrons, to picosec-
60 ond heating of the lattice ions, and subsequent hydrodynamic expansion into a vapor on
61 picosecond or longer timescales^{2,4-7}.

62 A common strategy uses electromagnetic radiation, often in the optical or UV range, to
63 deliver the intense energy burst. In such photonic experiments energy is delivered directly
64 to electrons, which then transfer energy to the ions (lattice) as the system relaxes toward a
65 state of local thermal equilibrium (LTE), a prerequisite for reaching local thermodynamic
66 equilibrium conditions. The timescale of equilibration between the ions and electrons is typ-
67 ically on the order order of ps^{6,8-10}. As electron-ion equilibration occurs roughly coincident
68 with the expansion, melting, and vaporization processes naturally coupled to lattice heating,
69 a loss of high-density conditions and sample confinement can occur before LTE is achieved,
70 leading to study of nonequilibrium matter exclusively. The experimental timescale is also
71 controlled by the size of targets, which in high power but low photonic-energy experiments is
72 limited by short radiation absorption lengths, even in dielectrics. Such practical challenges
73 of using radiation heating to study equilibrium warm dense matter in the laboratory often
74 complicate the experimental study of equilibrium extreme systems common in nature and
75 technology. Other methods of irradiative volumetric energy deposition providing access to

76 similar states of matter have similar limitations, include intense proton^{4,11}, heavy ion¹², and
77 electron⁸ beams. Dynamic compression, the driving of compression (i.e. shock or ramp)
78 waves traveling at near sound velocities ($\sim 1-10 \mu\text{m}/\text{ns}$)^{1,3,13-17}, is a somewhat slower form of
79 volumetric energy delivery, while diffusive¹⁸⁻²¹ (as opposed to ballistic^{2,5,22}) heat conduction
80 is even slower. While these latter approaches in principle provide better access to equilib-
81 rium states of warm dense matter, they are limited by restriction to adiabatic pathways
82 (dynamic compression) and by the aforementioned challenges of confining very hot matter
83 (diffusion).

84 One strategy to extend the lifetime of an irradiation-driven warm dense state is to provide
85 a tamper material around samples through which energy may be deposited and which delay,
86 prevent, or otherwise control expansion^{10-12,23-25}, such as by extending the time it takes
87 pressure release waves and cracks to propagate through the heated target. This tamping
88 approach can even confine the heated region entirely, enabling recovery of high density
89 samples quenched from conditions that would normally lead to vaporization²³. For optical
90 radiation, tamping can be achieved by placing an absorptive (i.e. metal) layer between
91 transparent (i.e. dielectric) tamper materials^{10,11,24}, by tightly-focussing the beam within
92 the tamper itself²³, or other configurations such as utilizing energetic electron transport
93 to deposit energy deeply in a target². However, tamping using high-power optical laser
94 irradiation is limited by the need to deliver sufficient energy through the tamper to the
95 sample, and thus depends on the optical transmission of the material under high brightness
96 radiation, often requiring thin tampers at all but the lowest irradiances¹⁰ which limit the
97 efficacy of this strategy. Targets of μm level thicknesses with experimental lifetimes of ps,
98 set by unconfined hydrodynamic expansion, remain common.

99 Intense x-rays also rapidly heat matter^{3,7,9,11,26-30}. This energy deposition may be intro-
100 duced deliberately (e.g. to heat or otherwise excite electrons in a sample) or may be a side
101 effect of probing samples with a high intensity x-ray beam. X-ray heating does not depend
102 on damage thresholds of targeted materials, as in optical laser experiments, but instead de-
103 pends nearly linearly on their x-ray absorption properties, which depend on atomic number
104 Z . For deliberate heating strategies, the potentially longer absorption lengths enable more
105 homogenous heating compared, e.g. to optical lasers or ion beams^{7,27,30}, and scaling up of
106 targets to enable larger irradiated volumes^{7,30}. X-ray heating performed with large opti-
107 cal laser^{11,30}, pulsed-power²⁵, and free electron laser (FEL)^{3,7,9,11,26,27,29} facilities has been

108 demonstrated. Many of these studies used lower photon energies (hundreds of eV to several
109 keV) which can still limit the potential thickness and materials of target components and
110 hence experimental timescales.

111 Free electron lasers and other high-brightness x-ray sources operating in the hard x-ray
112 regime above ~ 10 keV (Table I) allow for substantial scaling up of target dimensions and
113 experimental timescales. At x-ray energies exceeding ~ 10 keV, absorption lengths in even
114 heavy-element solids exceed several μm enabling large volume homogenous irradiation^{7,30}.
115 Moreover, x-ray absorption lengths are at the $\sim\text{mm}$ level above 10 keV in common light
116 element solids, allowing delivery of x-ray energy through thick low-Z tampers to high-Z
117 samples. The possibility of massive tampers which remain cold and stable during the exper-
118 iment, and which completely control the sample's expansion, may thus be realized with such
119 hard x-ray sources. For hard x-ray FELs, the high total pulse energy (~ 1 mJ, or 10^{12} pho-
120 tons), fast timescale (10-100 fs), and high intensity ($\sim 10^{18}$ W/cm²) is comparable to typical
121 optical laser systems; similar total energies in somewhat longer pulses (~ 100 ps) are possi-
122 ble at fourth-generation synchrotron radiation sources (Table I). In addition to presenting
123 challenges in adapting conventional x-ray probing studies to modern brilliant light sources,
124 these capabilities presage a new generation of irradiative extreme temperature experiments.
125 Radiatively heated samples in such experiments can, depending on target design, survive
126 longer than those in lower energy experiments, enabling the achievement and exploration
127 of more nearly thermal and thermodynamic equilibrium conditions, and study of processes
128 normally out of range in ultrafast experiments, such as diffusive heat conduction¹⁸⁻²¹, equi-
129 librium phase transformation¹⁷, and atomic-diffusion controlled processes including chemical
130 reaction, phase separation and mixing¹⁴. Moreover, a broader range of diagnostics may be
131 used to determine the sample state as experimental duration is increased, such as passive
132 pyrometry to determine sample temperature^{16,18-21,31} and hydrodynamic diagnostics^{16,29,32};
133 these would complement the wide range of available ultrafast measurements currently in
134 use, such as those based on probing with the same short-pulse x-rays^{17,29}.

135 Many interesting and poorly understood phenomena at warm dense matter conditions
136 are found at elevated densities, i.e. exceeding that of the solid state, including metallization
137 of molecular insulators³⁸ and phase separation in warm dense mixtures^{14,20,39}. To access
138 these conditions via irradiative heating requires that samples be initially pre-compressed
139 to the needed density. The effects of increasing density on fundamental interactions in

Facility	Pulse		X-ray Energy [keV]	Minimum Spot Size [μm]	Pulse Delay
	Duration [ps]	Energy [mJ]			
Hard X-ray Free Electron Lasers					
LCLS-II-HE ³³⁻³⁵	0.01-0.06	1-3	25 (12.8)	3	8.3ms (1 μs)
European XFEL	0.05 - 0.1	.35 - 4	5 - 20	< 1	220ns
SACLA ³⁶	0.01	0.5	4-15	1	17ms
Synchrotron Upgrades					
ESRF-EBS ³⁷	100	.04	10-70	0.15	176ns

TABLE I. Comparison of typical operating parameters of pulsed, focused x-ray facilities, with representative first-harmonic capabilities of current-generation XFELs and a representative 4th generation synchrotron upgrade.

140 irradiatively heated matter including bonding^{24,40} and electron-ion thermalization^{8,9,27} also
141 require investigation. The ability to employ confining tamper layers of substantial thickness
142 in hard x-ray experiments (if of sufficiently low-Z composition) raises the possibility of using
143 these layers as anvils to apply initial pressure to matter prior to x-ray probing or excitation.
144 Such a design is commonly used in static high pressure devices, notably the diamond anvil
145 cell (DAC), which employs thick (several mm) diamonds to isothermally compress thin
146 samples to high pressure and density⁴¹. Long-used at synchrotron facilities, and compatible
147 with hard x-ray illumination as either a probe or pump, the DAC offers the possibility to
148 study the properties and dynamics of high density, pressure and temperature material states
149 on ultrafast timescales when coupled to brilliant x-ray sources. Many x-ray measurements
150 developed for static high-pressure devices at traditional synchrotrons stand to be adapted
151 for use at modern higher-brightness sources, such as characterization of dynamic pressure
152 and temperature modulation^{18,42} with serial x-ray probing (Table I). Static compression
153 can also maintain sample confinement and high density during heating to the electron-
154 volt (>10,000 K) temperatures of warm dense matter²⁰, allowing near-isochoric experiments
155 orders of magnitude beyond hydrodynamic timescales.

156 The purpose of this study is several-fold, and motivated by the increasing brightness of
157 hard x-ray sources providing fast pulsed (nanosecond to femtosecond) hard x-rays (to tens
158 of keV) at high power (10^{11} - 10^{12} photons per pulse). The main objective is to explore the
159 thermal and mechanical evolution of pulse-irradiated targets involving particularly thick
160 tampers, a configuration suggested by the ability of hard x-rays to pass unimpeded through
161 low-Z tampers to a high-Z target layer confined within, to which energy is delivered. One
162 application of interest is extending isochoric radiative heating studies by delaying or inhibit-
163 ing altogether hydrodynamic expansion, so that matter can be observed at thermal, and
164 plausibly thermodynamic, equilibrium while at extreme temperature and near-solid density.
165 A related objective is to characterize the performance of diamond anvil high-pressure cells
166 (DACs), long used to great effect in synchrotron x-ray science, at higher intensity pulsed
167 x-ray sources where heating during the x-ray exposure could be an unavoidable byproduct of
168 x-ray probing or used deliberately to heat pre-compressed matter to extreme temperature,
169 as an alternative to optical laser heating^{18,20,41,43}. The response of the anvil-cell type of
170 tamped target to high brightness irradiation, and the designs it inspires for general tamped
171 laser-matter interaction experiments, are discussed in Sec. IV C. We also aim to character-
172 ize in general the heat dissipation in solid layered targets which may be of practical use as
173 beamline optics⁴⁴ and detectors⁴⁵ at x-ray facilities. The survival of these components often
174 depends on their heat and stress dissipation capabilities and often utilize high strength, high
175 thermal conductivity materials such as diamond^{44,45}.

176 II. METHODOLOGY

177 Targets simulated here consist of a sample layer or layers (μm thickness) between thick
178 (mm thickness) tampers. The advantages of this configuration are: (1) exceptionally long
179 confinement of samples at extreme conditions, so that the approach to, and properties of,
180 thermodynamic equilibrium states of high density and temperature can be studied; (2) effi-
181 cient control of sample temperature by using high thermal conductivity tampers, enhancing
182 sample stability and promoting sample survival after irradiation; and (3) the ability to
183 pre-compress samples with strong tampers, and resist thermomechanical stresses developing
184 during the irradiation.

185 The thermomechanical response of these micron-to-millimeter scale x-ray heated layered

186 targets evolves on a range of timescales. We consider a high-brightness monochromatic hard
 187 x-ray source, with a pulse duration similar to that available on modern FELs, delivering
 188 heat energy by x-ray absorption in ~ 100 fs over a beam spot ~ 10 μm in diameter. Pressure
 189 waves generated by thermal expansion propagate on ps-ns timescales, adiabatically mediat-
 190 ing pressure and temperature evolution in the differentially heated target; the timescale⁴⁶ is
 191 set by the scale length of the heated volume ℓ divided by the sound speed c , i.e. ℓ/c . Adia-
 192 batic conditions break down on ns- μs timescales, with heat conduction cooling heated areas
 193 toward the initial temperature, at which the surrounding target remains; the timescale⁴⁶ of
 194 this process is roughly the square of the heated volume size divided by the thermal diffusivity
 195 coefficient κ , or ℓ^2/κ . On these lengthscales (micron to millimeter) and timescales (ps and
 196 longer) LTE can be assumed, and target conditions develop primarily as a result of conven-
 197 tional hydrodynamic processes and diffusive heat transport in locally equilibrated matter;
 198 near-isochoric conditions are assumed to be maintained throughout by stable tampers.

199 To study heat conduction, we use a two-dimensional finite element (FE) model including
 200 conduction along and lateral to the x-ray beam path, both important on the associated (μs)
 201 timescales for tightly focussed radiation (Sec. II A). To study the hydrodynamic processes,
 202 which can take the form of shock discontinuities, we separately employ one-dimensional
 203 radiation hydrodynamics models to study the mechanical and associated thermal evolution
 204 of the system for the first few ns (Sec. II B); this approach is chosen because finite element
 205 models are not well suited to stress waves of larger magnitude, and because, if beam diameter
 206 is kept greater than the thickness of the relevant layers, the initial evolution of sample
 207 conditions is accurately treated as a one-dimensional process in the direction of the beam.

208 A. Finite Element Models

209 1. General approach

210 In order to describe the pulsed x-ray heating and cooling of a tamped sample configura-
 211 tion, we used a simulation software (COMSOL Multiphysics) based on finite element analysis
 212 to implement a two-dimensional, time-dependent heat transfer model^{19-21,46}, with semi-
 213 transparent materials exhibiting a bulk absorption of the x-ray radiation. We simulate the
 214 case of a single intense x-ray pulse of ~ 100 fs duration, and later (Sec. IV A) a train of such

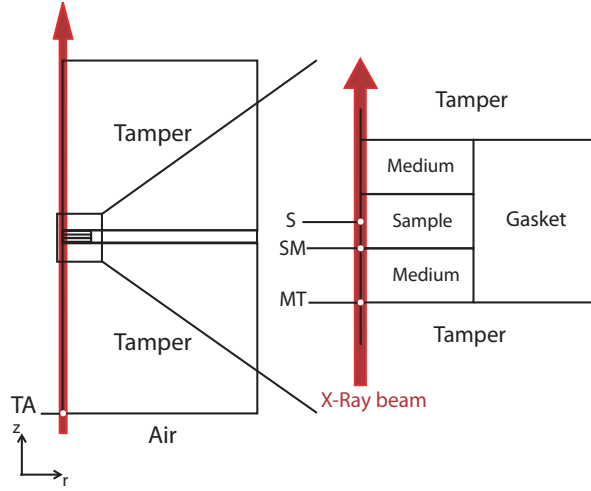


FIG. 1. Schematic illustration of the general model geometry, depicting the axis-symmetric slice from the axis to the edge of the cylinder. For finite element models, a 2D cylindrical geometry 160 μm in radius and 4005-4025 μm in length is employed. For hydrodynamic models a simple 1D representation of the boxed region is used. X-rays are incident from below. Standard dimensions are specified in Table II. Measurements are taken at S (sample center), SM (sample-medium interface), MT (medium-tamper interface), and TA (tamper-air interface), with interfaces referring to the leading (upstream) interface unless otherwise indicated.

215 pulses, striking a sample initially at room temperature (300 K).

216 Assuming a multilayer target of layers perpendicular to the incident x-ray beam (Fig.
 217 1), we exploit the symmetry around the beam, and consider a two-dimensional model by a
 218 rotational symmetry about an axis through the center of the beam path, with z referring to
 219 the axial position and r the radial position. The pulsed x-ray beam propagates in the $+z$
 220 direction, centered at $r = 0$. Including time t , this model is three dimensional. We vary the
 221 geometries of the layers used in the system as needed to simulate different configurations.
 222 Thick, low- Z tampers (or anvils) of 2 mm thickness are placed on either side of a primary
 223 sample ‘foil’ layer of 5 μm thickness. Additional interfacial layers (or medium), of several
 224 μm thickness, are used between the tamper and foil in most simulations. The medium can
 225 play several roles in experiments, acting as: (1) a protective layer, preventing direct heating
 226 of the tamper and absorbing thermal stress when resisting hydrodynamic expansion; (2) as
 227 an insulating layer to extend the experimental duration by limiting cooling of the sample;

228 and (3) as a hydrostatic pressure medium, in cases where the target is configured as a high
 229 pressure cell. The sample (and where used, medium) are contained laterally by a thick layer
 230 bridging the two tampers (or gasket, a component designed to reflect the configuration of
 231 anvil cells, which has little effect on the simulations). Typical dimensions are shown in
 232 Table II. This geometry is also symmetric about a parallel plane through the middle of
 233 the sample layer; conditions achieved, however, are asymmetric about this plane. Constant
 234 volume conditions are assumed, which is appropriate if targets remain in the condensed
 235 state (i.e. below vaporization points) or where they are configured to resist thermal stresses
 236 and hydrodynamic expansion, e.g. using thick tamper layers or an anvil cell design having a
 237 fixed sample cavity volume⁴³. The effects of thermal expansion and stress waves are treated
 238 separately as these occur on significantly different timescales and require a self-consistent
 239 hydrodynamic approach due to the rapid nature of heating and consequent shock production
 240 (Sec. II B).

Fixed Dimensions, Finite Element Models	
Parameter	Value[μm]
Model Domain Radius	160
Foil Radius	40
Medium Radius	40
Tamper Thickness (d_T)	2000
Foil Thickness (d_S)	5

TABLE II. Geometric constant parameters for finite element modeling.

241 In order to describe the dynamical temperature evolution of targets, we used the finite-
 242 element solution of the time-dependent energy transfer equation. The volumetric heat source
 243 $Q(r, z; t)$ (the net energy generated per unit volume and time) representing the radiative
 244 energy absorbed within the target is given as

$$245 \quad Q(r, z; t) = \rho C_P \frac{\partial T}{\partial t} + \nabla \cdot (-k \nabla T), \quad (1)$$

246 where T is the temperature, t is the time, k is the thermal conductivity, ρ is the density,
 247 and C_P is the heat capacity at constant pressure. For constant physical properties, and
 248 considering the period after heating, Eq. 1 reduces to

$$249 \quad \frac{\partial T}{\partial t} = \kappa \nabla^2 T, \quad (2)$$

250 where κ is the thermal diffusivity,

$$251 \quad \kappa = \frac{k}{\rho C_P}. \quad (3)$$

252 Radiative (photon) heat transfer is generally negligible compared to diffusive (phonon and
 253 electron) heat conduction at the presently examined temperatures and timescales⁴⁶, and is
 254 not included.

255 The source term $Q(r, z; t)$ (typical units of W/m^3) is given by volumetric heat generation
 256 when the incident x-ray beam passes through, and is absorbed within, the semi-transparent
 257 materials. Due to this absorption the beam intensity decays exponentially with depth (Beer-
 258 Lambert law). At the considered x-ray energies, the contribution of diffuse scattering to total
 259 attenuation is small and is neglected in our calculations. Coherent scattering (i.e. Bragg
 260 diffraction) could become important particularly where thick single crystals are used as
 261 tampers, affecting attenuation and radiation trajectory, though, as it can be avoided in
 262 practice⁴⁷, it is also ignored. The energy deposition in a given homogenous layer in a target
 263 can thus be written as

$$264 \quad Q(r, z; t) = I_s(r; t) \alpha (1 - R_s) \exp[-\alpha(z - z_s)] \quad (4)$$

265 where α is the absorption coefficient, constant in the layer, z_s is the z position of the
 266 layer surface the radiation is incident on, R_s is the reflectivity of the leading surface or
 267 interface, and $I_s(r; t)$ is the incident intensity on the surface (typical units of W/m^2). For
 268 x-ray radiation, reflectivities of interfaces are exceedingly small, of order $R_s \sim 10^{-9} - 10^{-13}$,
 269 and may be neglected. Thus the attenuation of x-rays as well as the energy deposition is
 270 accurately estimated by considering absorption only.

271 The absorption in the target is given by computing the sequential absorption in several
 272 such layers. At the downstream surface of a layer, boundary conditions establish that any
 273 light reaching that boundary will leave the domain and pass to the next layer and this is
 274 repeated until the beam reaches the downstream target surface and leaves the geometry.

Pulse Parameters, Finite Element Models	
Parameter	Value[units]
Arrival time (μ)	400[fs]
Pulse length (σ_t)	100[fs]
Pulse size (σ_r)	5[μm]

TABLE III. Parameters for the x-ray pulse in finite element models.

275 For example, in the center of the sample (and target), we have

$$276 \quad Q(r = 0, z = z_c; t) =$$

$$277 \quad I(r; t) \alpha_S \exp(-\alpha_S \frac{d_S}{2}) \exp(-\alpha_M d_M) \exp(-\alpha_T d_T), \quad (5)$$

278 where S , M , and T refer to the sample, medium, and tamper values, respectively, $I(r; t)$ is
279 the incident intensity on the target assembly, d refers to the thickness of particular layers,
280 and z_c refers to the center of the sample layer (and target assembly), hence only half of the
281 sample's thickness is included.

282 The model considers heating induced during a ~ 100 fs duration x-ray pulse, and the con-
283 ductive heat transfer following the rapidly imposed temperature distribution in the target.
284 The heating pulse intensity is assumed to follow a Gaussian distribution in time and space,
285 with incident intensity $I(r; t)$ (Eq. 6) reaching a maximum, I_{max} , at $t = \mu$ and $r = 0$ as

$$286 \quad I(r; t) = I_{max} \exp\left[-\frac{r^2}{2\sigma_r^2}\right] \exp\left[-\frac{(t - \mu)^2}{2\sigma_t^2}\right], \quad (6)$$

287 where σ_r is a Gaussian radius parameter, such that the FWHM (full width at half maximum)
288 diameter of the pulse is

$$289 \quad \text{spot size} = 2\sqrt{2 \ln 2} \sigma_r, \quad (7)$$

290 and σ_t defines the temporal width of the pulse (FWHM) as

$$291 \quad \text{pulse duration} = 2\sqrt{2 \ln 2} \sigma_t. \quad (8)$$

For the parameters of this simulation (Table III) the spot size is then $\sim 12 \mu\text{m}$, and the
pulselength ~ 240 fs. The incident peak intensity I_{max} can be related to the net energy of

the single pulse E_{pulse} (in J), the peak incident power P_{max} (in W, and occurring at $t = \mu$), and the peak energy density per area Λ_{max} (in J/m², and occurring at $r = 0$) as

$$I_{max} = \frac{E_{pulse}}{(2\pi)^{\frac{3}{2}}\sigma_t\sigma_r^2} \quad (9)$$

$$= \frac{P_{max}}{2\pi\sigma_r^2} \quad (10)$$

$$= \frac{\Lambda_{max}}{(2\pi)^{\frac{1}{2}}\sigma_t} \quad (11)$$

292 The number of photons per pulse N is

$$293 \quad N = \frac{E_{pulse}}{E_{photon}} \quad (12)$$

294 and is equivalent to $\sim 10^{12}$ for the peak energy per pulse (3.5 mJ) and x-ray energy (25
 295 keV) simulated here, which are close to the facility maxima (Table I). In our models we
 296 specify E_{pulse} (Eq. 9), which when integrated over the pulse duration (Eqs 5 and 6) leads to
 297 $Q(r, z; t \gg \mu)$ independent of the pulse duration, such that $T(r, z)$ immediately after the
 298 pulse (and before significant heat transport occurs) depends only on total pulse energy and
 299 its spatial distribution, i.e. temperature achieved is independent of pulselength so long as
 300 the pulselength is shorter than heat conduction timescales. This implies any pulse duration
 301 less than the heat conduction timescales (roughly in the ns range or less) will achieve similar
 302 peak temperature and show identical cooling behavior.

303 The initial temperature of the entire system is assumed to be ambient (300 K). As a
 304 boundary condition, the external surface of the simulation cell shown in Fig. 1 was given by
 305 natural heat exchange with a surrounding atmosphere (air), with the external temperature
 306 fixed at 300 K, and heat loss from the surface determined as

$$307 \quad q_0 = h(300 \text{ K} - T) \quad (13)$$

308 where q_0 is the convective heat flux and h is the convective heat transfer coefficient ($h =$
 309 5 W/m²/K, for natural convection in air). This has no significant effect for the cooling
 310 timescale of these experiments; similar results could be expected in vacuum.

311 A free triangular mesh is employed, which is kept very fine at interfaces due to the need
 312 to stabilize the model during the initial phase of large temperature gradients at interfacial
 313 regions, at heating times 10^{-12} to 10^{-9} s; the heat transfer starts at approximately on 10^{-9}
 314 s time scales, and temperature is stable before this if the simulation is configured properly.

315 A coarser mesh is used away from the interfaces. The accurate modeling of interfaces on
316 shorter timescales is validated analytically (Sec. III A 8).

317 As the simulations seek to establish general trends for the effects of target composition,
318 geometry, and beam parameters, a number of physical assumptions are made in our calcula-
319 tions. We assume a direct relationship between the amount of x-ray energy deposited in the
320 target at a given location and the amount of heating at this location. Further, the models
321 assume that thermal equilibrium (i.e. between electrons, which initially absorb energy, and
322 ions, which heat more gradually on the ps timescale of electron-ion equilibration) occurs
323 instantly. Thus our simulations should be accurate at timescales where electron-ion equi-
324 librium has been achieved ($t \gg 10^{-12}$ s), while only approximating the initial (fs) heating
325 process. Implicitly, we also assume localization of hot electrons during the equilibration
326 period, i.e. that any hot electrons produced ultimately equilibrate with nearby ions. This is
327 a reasonable approximation since the typical mean free path of ballistic hot (eV) electrons
328 in condensed matter tends to be of order $10^{-2} \mu\text{m}^{11,27,40}$, which is much less than the sample
329 dimensions and heating beam diameter ($1\text{-}10^3 \mu\text{m}$), consistent with a diffusive heat transfer
330 model being sufficiently accurate on these time and lengthscales. While not included here,
331 hydrodynamic (Sec. II B) and radiative processes, longer-distance hot electron transport
332 (e.g. Refs. 2,15), and nonlinear absorption due to high x-ray fluence or short timescale e.g.
333 resulting from mass ejection of core electrons²⁸ and saturation of absorption²⁷, can modify
334 initial temperature distributions, but cooling behavior will be similar. With a propagation
335 time across the entire target of $\sim 10^{-11}$ s, it suffices for our purposes to assume the x-ray
336 beam is incident in all points of the target simultaneously.

337 2. *Materials parameters*

338 A suite of materials with varying properties are included in the models to examine the
339 possible range of heating and cooling behavior under x-ray irradiation. As the degree of
340 x-ray absorption in a substance is roughly given as

$$341 \quad \alpha \propto \frac{\rho Z^4}{A E_{\text{photon}}^3} \quad (14)$$

342 where atomic number and mass are Z and A respectively, we sought to explore samples over
343 a wide range of Z , and lesser variances in the surrounding low- Z materials, as well as a range

Standard Configuration, Finite Element Models					
Medium Thickness[μm]	Materials			Photon	Energy/ Pulse[mJ]
	Sample	Medium	Tamper	Energy[keV]	
5	Fe	Al ₂ O ₃	Diamond	25	0.35
Varying Configurations, Finite Element Models					
Medium Thickness[μm]	Materials			Photon	Energy/ Pulse[mJ]
	Sample	Medium	Tamper	Energy[keV]	
0,	Fe,		Diamond,	25,	3.5,
2,	H ₂ O,	Al ₂ O ₃ ,	Be,	20,	0.35,
5,	Mo,	LiF,	Graphite,	15,	35,
10	Pb,	Ar	Al ₂ O ₃ ,	10,	3.5
	Gd ₃ Ga ₅ O ₁₂		Kapton	5	

TABLE IV. Model input parameters, with standard configuration at top and sets of varying simulation parameters explored shown at the bottom.

344 of photon energy which has a similarly strong effect on absorbance. Material properties are
345 assumed to be constant with temperature, in order to provide a representative and simplified
346 picture of material response for a range of possible materials. More detailed materials
347 modeling could include temperature (and pressure) sensitivity of parameters, effects of phase
348 transformations, and effects of electronic excitations (e.g. electronic heat capacity⁴⁸), for
349 example. These models thus provide a representative picture of the lifetime and properties
350 of hot states in strongly-tamped targets following a comparatively rapid emplacement of
351 equilibrium temperature by irradiation. All material properties are taken to be isotropic;
352 material anisotropy may need to be accounted for when there are strong variations in relevant
353 properties with direction, such as in thermal conductivity⁴⁹.

354 The model calculations were performed most commonly with a standard material sys-
355 tem comprising a primary sample of iron, a surrounding medium of alumina (Al₂O₃), and
356 diamond as the tamper (Tables IV and V). This standard assembly was then explored by

Standard Material Parameters, Finite Element Models								
	Thermodynamic Properties			Photo absorption coefficient α [1/m]				
Material	ρ	C_P	k	25	20	15	10	5
	[kg m ⁻³]	[J (kg K) ⁻¹]	[W (m K) ⁻¹]	[keV]	[keV]	[keV]	[keV]	[keV]
Fe	7870	450	60	1.03×10^4	1.95×10^4	4.40×10^4	1.33×10^5	1.05×10^5
Al ₂ O ₃	3975	765	46	4.32×10^2	8.04×10^2	1.86×10^3	6.23×10^3	4.82×10^4
Diamond	3520	630	1500	9.10×10^1	1.28×10^2	2.40×10^2	7.69×10^2	6.68×10^3

TABLE V. Materials parameters used in FE calculations for standard sample configuration.

357 varying independently the x-ray energy (Tables IV and V), beam power (Table IV), the
 358 materials comprising the sample, medium, and tamper (Tables IV and VI), and the medium
 359 layer thicknesses (Table IV). Sample materials were chosen to represent a range of possible
 360 x-ray absorption levels, including a range of metals across a range of Z (Fe, Mo, Pb), a
 361 representative low-Z material (H₂O) which is also an insulator, and a representative high-Z
 362 insulator (gadolinium gallium garnet, Gd₃Ga₅O₁₂, or ‘GGG’). The additional material at
 363 the outside edge of the sample area, referred to as a gasket, is composed of rhenium (Table
 364 VI). Representative thermo-physical and optical bulk material parameters (Tables V and
 365 VI) were taken from values measured at ambient pressure and temperature, unless otherwise
 366 noted. X-ray photon energies were taken from the hard x-ray regime typically available and
 367 used at FEL sources in x-ray diffraction and absorption measurements. Pulse power (given
 368 in terms of total pulse energy) was taken to peak near the maximum presently available at
 369 such facilities.

370 Diamond was selected as an ideal tamper due to its high x-ray transparency, high ther-
 371 mal conductivity, and high strength to withstand mechanical stresses generated by heating
 372 or pre-compressing samples, as in a diamond anvil cell⁴³. Diamond has an extremely high
 373 mechanical damage threshold beyond that of all known substances¹³ with ability to with-
 374 stand localized stresses exceeding a TPa⁵⁰. It has the highest thermal conductivity of all
 375 known bulk matter, allowing it to act as an excellent heat sink which, when properly con-
 376 figured, allows the tamper to remain at very low temperature even when adjacent to very

Additional Material Parameters, Finite Element Models				
	Thermodynamic Properties			Absorption
	ρ	C_P	k	coefficient (25 keV)
Material	$[\text{kg m}^{-3}]$	$[\text{J (kg K)}^{-1}]$	$[\text{W (m K)}^{-1}]$	$[\text{1/m}]$
H ₂ O	1000	4187	0.686	4.34×10^1
Mo	10188	251	113	4.63×10^4
Pb	11340	140	30	5.28×10^4
Gd ₃ Ga ₅ O ₁₂	7080	381	11	1.32×10^4
LiF	2639	1562	11	1.18×10^2
Ar ^a	5550	570	60	2.46×10^3
Be	1848	1825	201	3.14×10^1
Graphite	2210	830	470	5.71×10^1
Kapton	1420	1095	0.46	4.36×10^1
Re	21020	140	48	... ^b

^aProperties taken for high pressure solid Ar, as used in anvil cells¹⁹.

^bValue not used in the simulation.

TABLE VI. Parameters for other materials used in FE models, including the different materials tested for the sample, medium and tamper, and that used in the gasket.

377 high temperature matter^{20,43}. Metastable at ambient conditions, and only thermodynam-
378 ically stable under pressures exceeding ~ 13 GPa at room temperature, it is generally at
379 risk of damage from thermal decomposition processes such as oxidation and graphitization
380 at temperatures exceeding ~ 1000 K, as well as non-thermal graphitization at high x-ray
381 fluence⁴⁰. Even under high pressure where diamond is stable, it will melt at sufficiently high
382 temperature¹⁶. Several other plausible tamper materials are considered which can provide
383 qualities including competitive mechanical strength behavior (Al_2O_3), superior x-ray trans-

384 parency (Be, Kapton), resistance to thermal degradation and stability over a wide range
 385 of temperature (Be, Al₂O₃, Graphite), and relatively good thermal conductivity within an
 386 order of magnitude of that of diamond (Be, Graphite) as well as extremely low thermal
 387 conductivity where thermal confinement rather than dissipation may be desired (Kapton).

388 Absorption edges were avoided for the selected materials at the studied x-ray energies.
 389 However, the sudden increases in absorbance with increasing photon energy can have a
 390 major effect on the achieved conditions in experiments. Experiments deliberately or inci-
 391 dentally targeting near-edge conditions, e.g. to study edge structure, might be particularly
 392 susceptible to complications. These include irregular heating if x-ray energy is not purely
 393 monochromatic and varies from pulse to pulse; for example, an energy instability within a
 394 bandwidth of $\sim 10^{-3}$, typical of XFEL SASE sources, exceeds the width of absorption edges
 395 in the keV range and can lead to stochastic heating near edges.

396 B. Hydrodynamic Models

397 As the temperature is increased in the targets, hot areas are subject to thermally-driven
 398 expansion, and local stresses can develop which are roughly proportional to the amplitude
 399 of the temperature change. On short timescales (fs-ps), heating is fully isochoric, or nearly
 400 so. On the longer term (ps-ns), expansion⁷ and the concomitant production of stress-density
 401 waves will occur. In the limiting case of isochoric heating and assuming hydrostatic stress
 402 and LTE conditions, we can consider the thermodynamic identity

$$403 \quad \left(\frac{\partial P}{\partial T} \right)_V = \beta K_T \quad (15)$$

404 where β and K_T are the volumetric thermal expansivity and isothermal bulk modulus,
 405 respectively. This implies an isochoric thermal pressure change ΔP_V , for a given imposed
 406 temperature change ΔT , as

$$407 \quad \Delta P_V \simeq \beta K_T \Delta T. \quad (16)$$

408 With K_T of order 1 - 10³ GPa and $\beta \simeq 10^{-5}$ K⁻¹ for condensed matter, and considering max-
 409 imum achieved temperatures in the range of 10³-10⁵ K, thermal stresses produced in typical
 410 experiments can reach values between 10⁻² and 10³ GPa, compatible with the creation of
 411 high pressure shock waves.

412 In an unconfined target, the expansion of the heated sample via pressure waves can reduce
 413 the amplitude of dynamic stress to zero; for a tamped target free expansion is prevented
 414 leading to a more complex system of compression and release. We have employed the HYADES
 415 hydrocode⁵¹ to study the 1D evolution of the stress, strain, and temperature in the adiabatic
 416 initial part of the experiment following heating. Experiments are initialized at $T=300$ K
 417 and ambient pressure and density for the different target layers. We use tabular equations
 418 of state (Sesame 7830 for diamond, Sesame 2980 for Mo, and Sesame 7410 for Al_2O_3) in
 419 the models. We model only the first several μm of the tamper closest to the sample; where
 420 wave interactions with simulation cell boundaries produce unphysical conditions, very late
 421 in the simulation, the results are removed. An average atom ionization model is used to
 422 generate opacities. The calculations exclude electron-ion nonequilibrium (electron and ion
 423 temperatures are always equal); thermalization should occur rapidly⁵² compared to bulk
 424 hydrodynamic processes in a target of this size, where shock durations are of order hundreds
 425 of picoseconds. We also have not included 2D effects, which would be needed to accurately
 426 describe the later-time behavior of this system (roughly as wave propagation distances exceed
 427 the beam radius).

428 III. RESULTS

429 A. Finite Element Heat Transfer Results

430 1. *Standard configuration*

431 The baseline simulation, on which other simulations are perturbations, uses the standard
 432 target materials arrangement, radiation of 25 keV and a net pulse energy of 0.35 mJ (Fig.
 433 2). A close-up view of the sample region (Fig. 3) shows the development of temperature
 434 gradients, from an initial state of nearly-constant temperature within layers (at given r) and
 435 discontinuities at layer interfaces. The diamond tamper in this case, by virtue of its high
 436 thermal conductivity, provides rapid quenching of the tamper itself by radial heat flow, while
 437 the sample region remains hot on longer timescales (Fig. 3). Initial radial gradients (imposed
 438 by the assumed Gaussian beam profile) are roughly preserved and somewhat broadened with
 439 time [Fig. 2(c)]. Note the sudden rise in temperature at the medium-tamper interface just
 440 before 10^{-6} s [Fig. 2(b)], corresponding to arrival of a heat wave from the sample moving

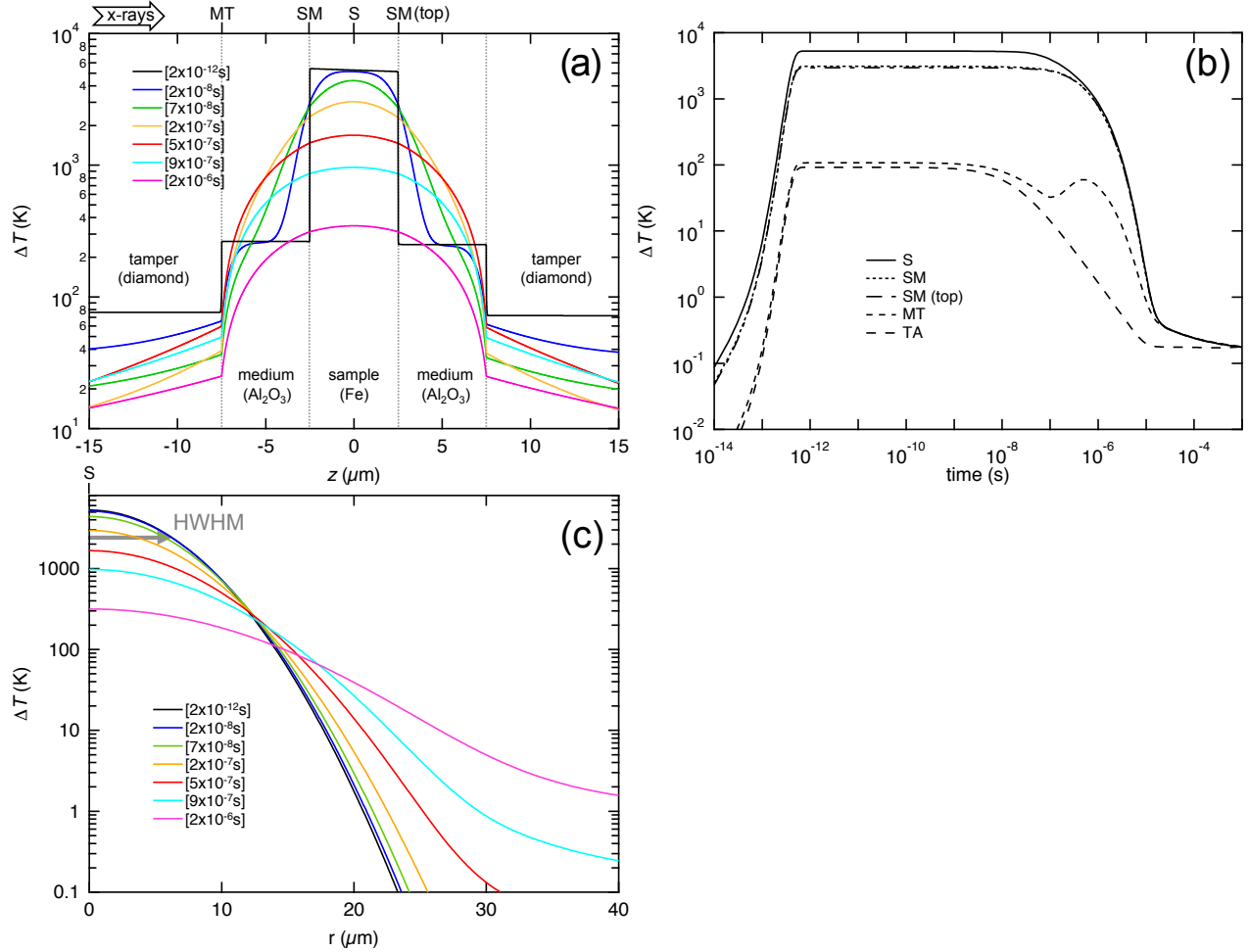


FIG. 2. Thermal response of the baseline simulation. (a) Temperature change vs. position along the beam path center ($r = 0$) in the sample region. (b) Temperature change vs. time at (see Fig. 1) sample center (S), leading (SM) and trailing (SM top) sample-medium interfaces, leading medium-tamper interface (MT), and leading tamper free surface (TA). (c) Radial temperature distribution at the center of the sample, showing the half-width at half maximum (HWHM) of the beam and initial temperature distribution (black). Here and elsewhere, times are given in the square brackets.

441 across the medium.

442 2. Radiation variance: X-ray intensity

443 Varying the beam intensity (Fig. 4) proportionally shifts the thermal response of the
 444 target components, a result of the assumed linear absorption process and temperature in-

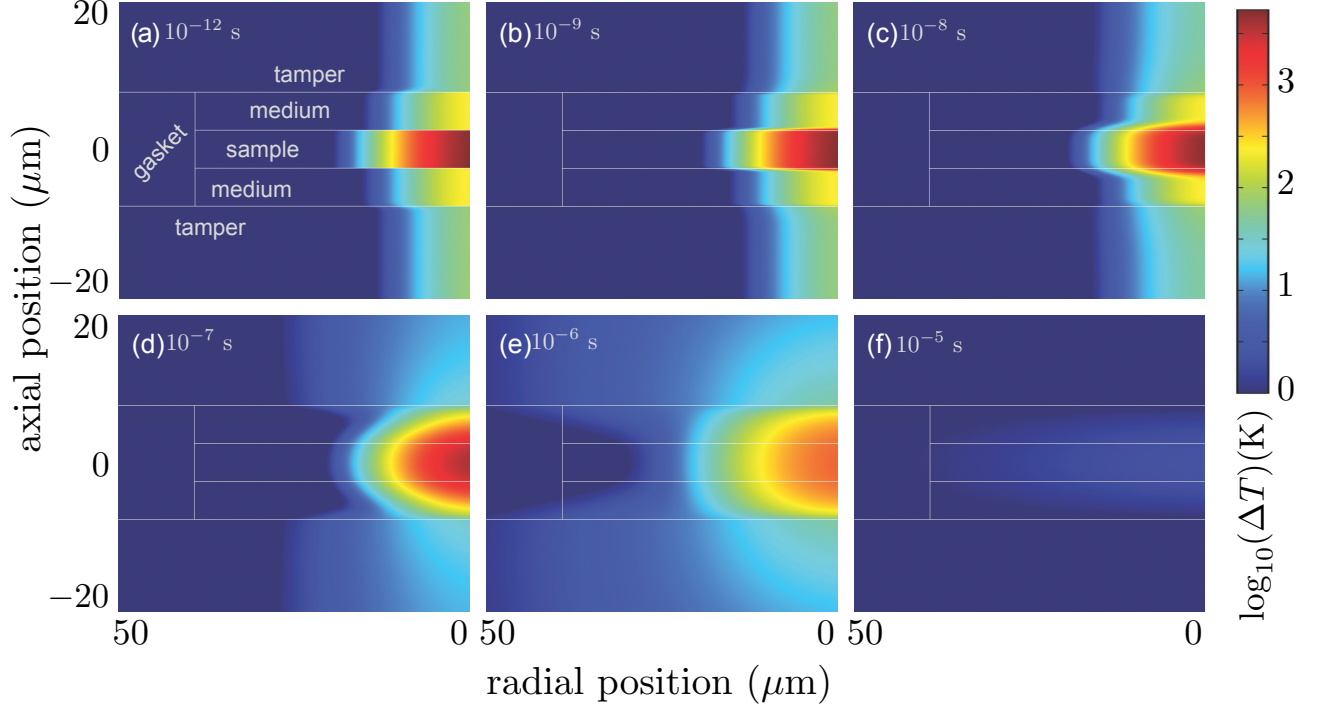


FIG. 3. Temperature change map in the $r-z$ plane for the standard experiment at different times, showing the detailed behavior of the sample area. Lines show the boundaries between sample components (see Fig. 1).

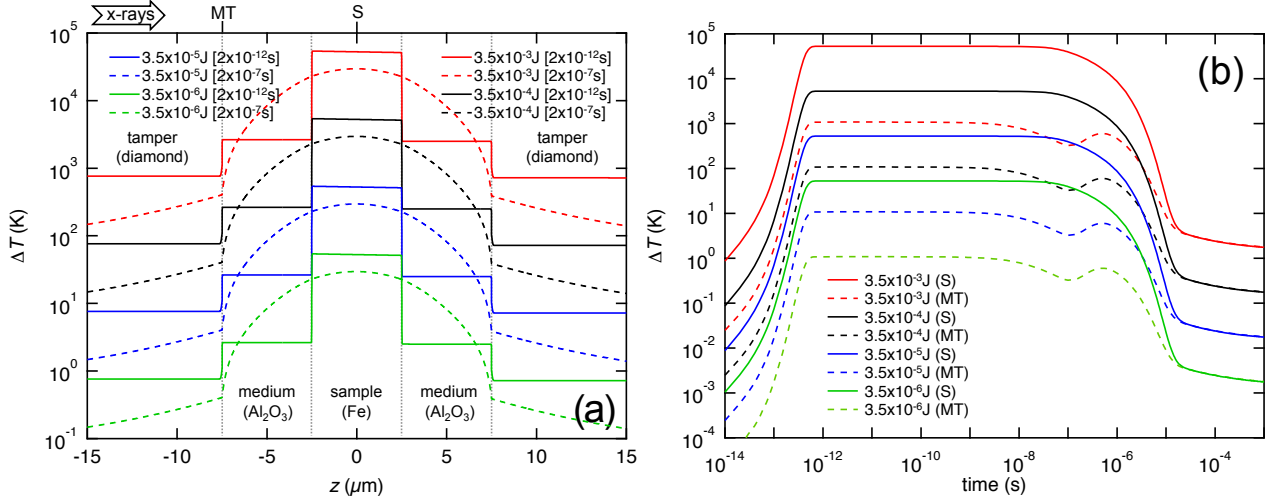


FIG. 4. Variance of thermal response with x-ray fluence (energy per pulse). (a) Temperature change vs. position along the beam path center ($r = 0$) in the sample region. (b) Temperature change vs. time at sample center (S) and leading medium-tamper interface (MT). The black lines correspond to the standard simulation. Times are given in square brackets in seconds.

445 sensitive material parameters. Thus, as rule of thumb, the temperature change at any x-ray
 446 fluence can be computed from a given simulation's ΔT^{sim} by scaling to the ratio of the x-ray
 447 fluencies, i.e.

$$448 \quad \Delta T = \frac{I_{max}}{I_{max}^{sim}} \Delta T^{sim}. \quad (17)$$

449 **3. Radiation variance: X-ray photon energy**

450 Varying the x-ray wavelength (photon energy) through the hard x-ray range will vary
 451 the differential absorption in samples, and the temperature gradients established (Fig. 5).
 452 For lower energies (~ 5 keV) the x-ray is absorbed almost entirely within the leading tamper
 453 layer [Fig. 5(c),(e)] whereas harder x-rays (~ 25 keV) will largely pass through the sample
 454 assembly without generating much heating. Homogeneity of heating depends on the x-ray
 455 energy, with harder x-rays producing superior initial homogeneity and lower energies greater
 456 initial asymmetry [Fig. 5(a)]. In terms of providing an optimum heating solution, a 15 keV
 457 energy provides maximum sample heating, nearly homogeneous temperature in the sample
 458 and moderate but survivable heating in the tamper.

459 **4. Geometry variance: Medium thickness**

460 Without an interfacial medium layer between the sample and tamper, the temperature
 461 of the tamper is maximized by direct exposure to the hot sample; the sample is also cooled
 462 rapidly, but the tamper interface remains relatively hot (Fig. 6). Addition of even a thin
 463 medium layer reduces the temperature in the tamper considerably, while slowing sample
 464 cooling. When a medium is present, sample cooling behavior is insensitive to medium layer
 465 thickness, up to $10^{-7} - 10^{-6}$ s, after which it varies considerably. Tamper cooling also
 466 proceeds more rapidly for a thicker medium layer. Arrival of the heat wave from the sample
 467 [Fig. 6(b) at $\sim 10^{-6}$ s] can briefly drive tamper interfacial temperatures higher, possibly to
 468 above the initial temperature, though this temperature excursion remains below that which
 469 would occur in the absence of the medium. Thus, addition of even a thin medium layer can
 470 reduce heating of the tamper and potentially improve its stability.

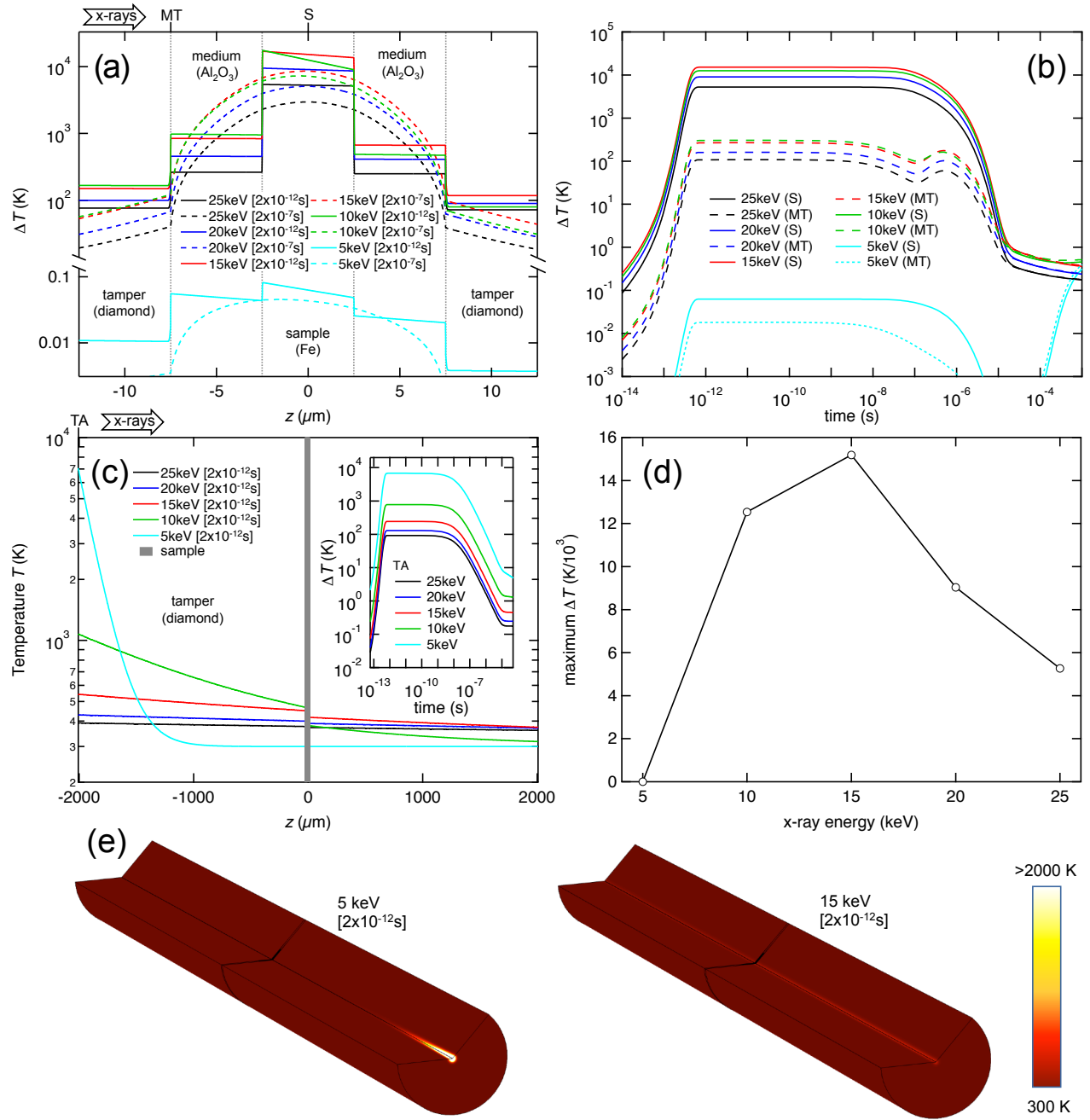


FIG. 5. Variance of the thermal response with x-ray photon energy. (a) Temperature change vs. position along the beam path center ($r = 0$) in the sample region. (b) Temperature change vs. time at sample center (S) and leading medium-tamper interface (MT). (c) Absolute temperature vs. position along the beam path center ($r = 0$) across the whole target, with inset showing temperature change vs. time at the leading tamper free surface (TA). (d) Maximum temperature increase at sample center (S) as a function of photon energy. (e) Cylindrical simulation region temperature immediately after heating for 5 keV (left) and 15 keV (right). The black lines in (a)-(c) correspond to the standard 25 keV simulation results. Times are given in square brackets in seconds.

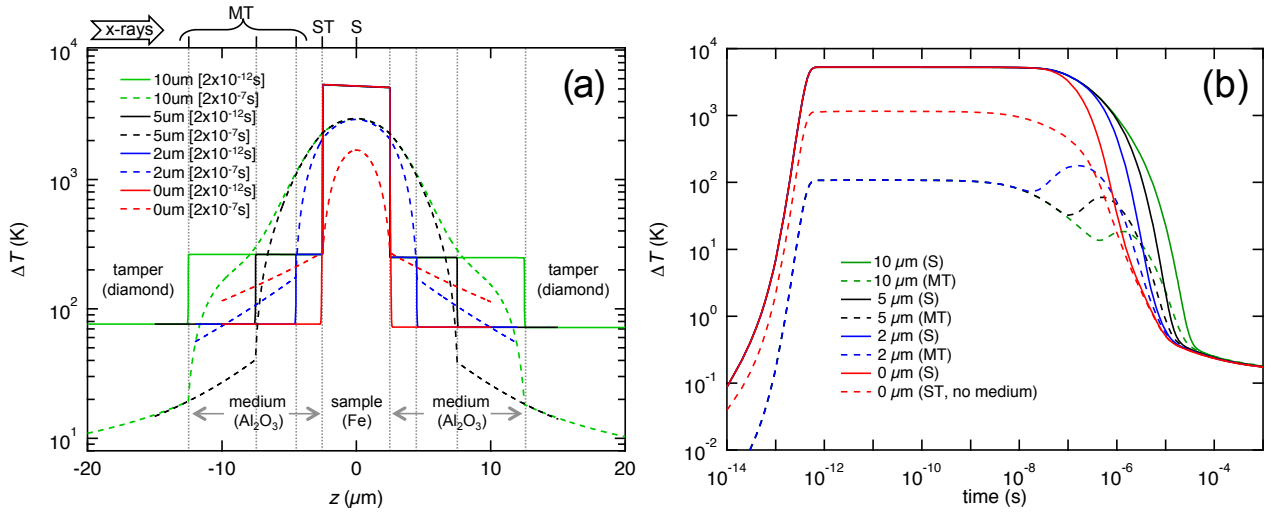


FIG. 6. Variance of thermal response with interfacial layer (medium) thickness. No layer (direct contact of sample and tamper) corresponds to red. (a) Temperature change vs. position along the beam path center ($r = 0$) in the sample region. (b) Temperature change vs. time at sample center (S) and at the leading medium-tamper interface (MT), or sample-tamper interface (ST) in the absence of a medium layer. The black lines correspond to the standard simulation. Times are given in square brackets in seconds.

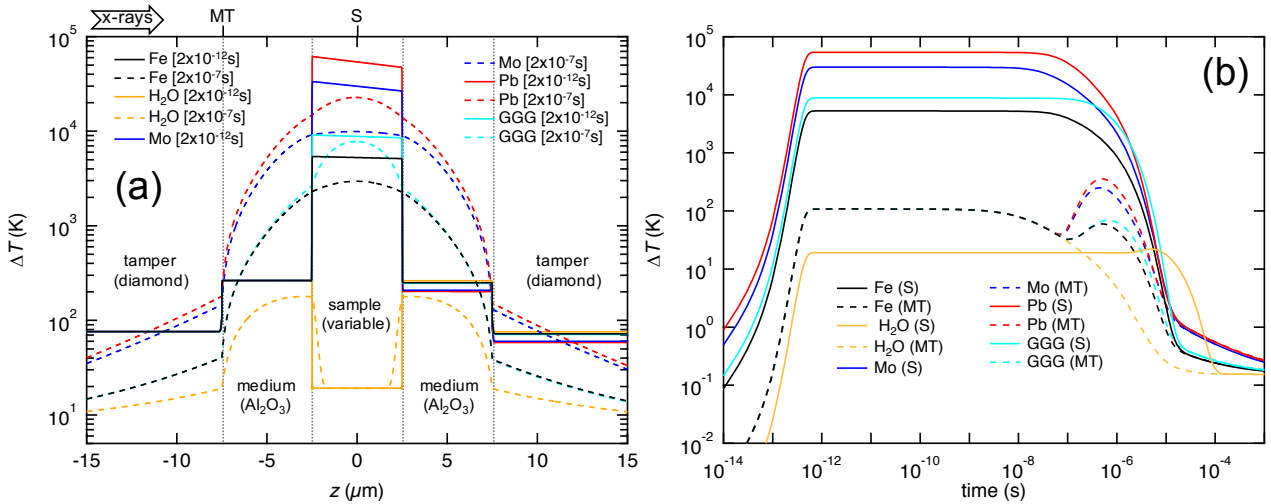


FIG. 7. Variance of thermal response with sample material. (a) Temperature change vs. position along the beam path center ($r = 0$) in the sample region. (b) Temperature change vs. time at sample center (S) and leading medium-tamper interface (MT). The black lines correspond to the standard simulation. Times are given in square brackets in seconds.

471 **5. *Material variance: Sample***

472 The samples were generally selected (Fig. 7) to exhibit the strongest heating of all
473 target components, and are hence higher-Z materials, with the exception of water which has
474 exceptionally weak heating, below all the other target components. Electrically insulating
475 samples H₂O and the heavy oxide Gd₃Ga₅O₁₂ (which heats similar to Fe) have reduced
476 thermal conductivities compared to the metals Fe, Mo, and Pb (Table VI), which slow their
477 thermal evolution during the experiments, effectively maintaining the sample temperature
478 even while metals cool off (Fig. 7). Heat waves incident on the tamper, at around 10⁻⁶ s,
479 cause large jumps in tamper surface temperature to well in excess of its initial temperature
480 for hotter samples [Fig. 7(b)]. For water, heat conducts into the sample from the hotter
481 medium layers, leading to a late increase in temperature for this sample. At this x-ray energy
482 (25 keV) the absorbance of each material is small such that the downstream temperatures
483 are only weakly affected by the different samples [right side of Fig. 7(a)]. Initial asymmetries
484 in temperature in the sample area are more pronounced for the higher Z samples [Fig. 7(a)].

485 **6. *Material variance: Tamper***

486 The tampers chosen for modeling (Fig. 8) generally show comparable x-ray transparency,
487 with the exception of Al₂O₃ which has somewhat reduced transmission and hence results
488 in lower sample temperature and higher tamper body temperatures. There is significant
489 variance in the temperature and its evolution in the tamper bodies [Fig. 8(c) inset], but
490 on shorter timescales sample conditions do not evolve differently for the different tampers
491 [Fig. 8(a)-(b)]. Significant differences in sample temperature evolution are observed only on
492 long (> 10⁻⁶ s) timescales [Fig. 8(b)]. For the comparably low thermal conductivity plastic
493 (Kapton) tamper, an accumulation of heat at the tamper interface is observed [Fig. 8(a)],
494 which could promote tamper damage.

495 **7. *Material variance: Medium***

496 The interfacial medium layer material selected (Fig. 9) influences the sample temper-
497 ature by controlling the rate of sample cooling, which is most notable on longer (> 10⁻⁶
498 s) timescales. As all media chosen are of low x-ray absorbance, differences in performance

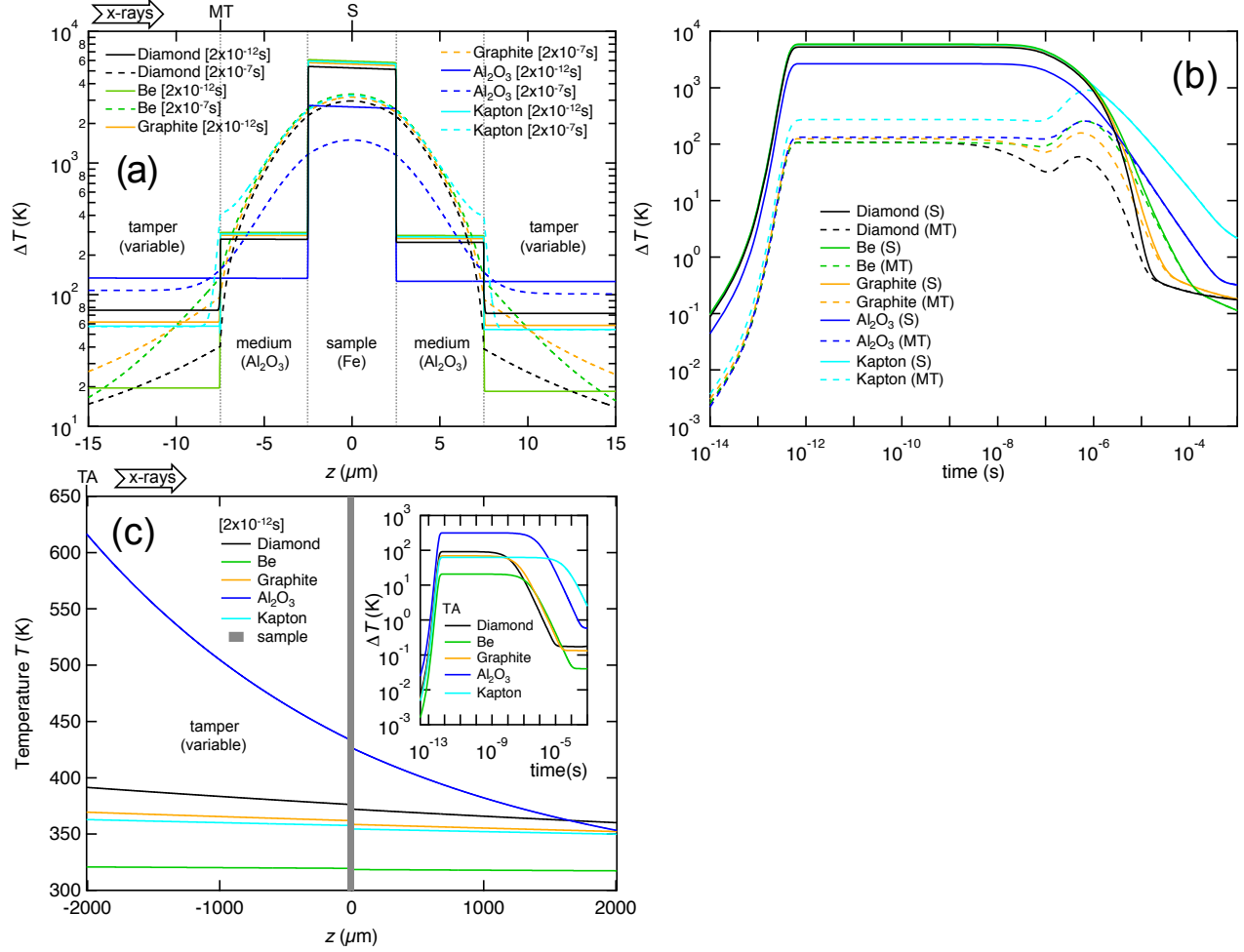


FIG. 8. Variance of thermal response with tamper material. (a) Temperature change vs. position along the beam path center ($r = 0$) in the sample region. (b) Temperature change vs. time at sample center (S) and leading medium-tamper interface (MT). (c) Absolute temperature vs. position along the beam path center ($r = 0$) across whole target, with inset showing temperature change vs. time at the leading tamper free surface (TA). The black lines correspond to the standard simulation. Times are given in square brackets in seconds.

499 are due mainly to the thermal conduction properties of the medium layers. Sample cooling
 500 is most sluggish for the lowest thermal conductivity medium (LiF), even though the initial
 501 temperature of this layer is also the lowest (which promotes more rapid cooling, all else
 502 being equal).

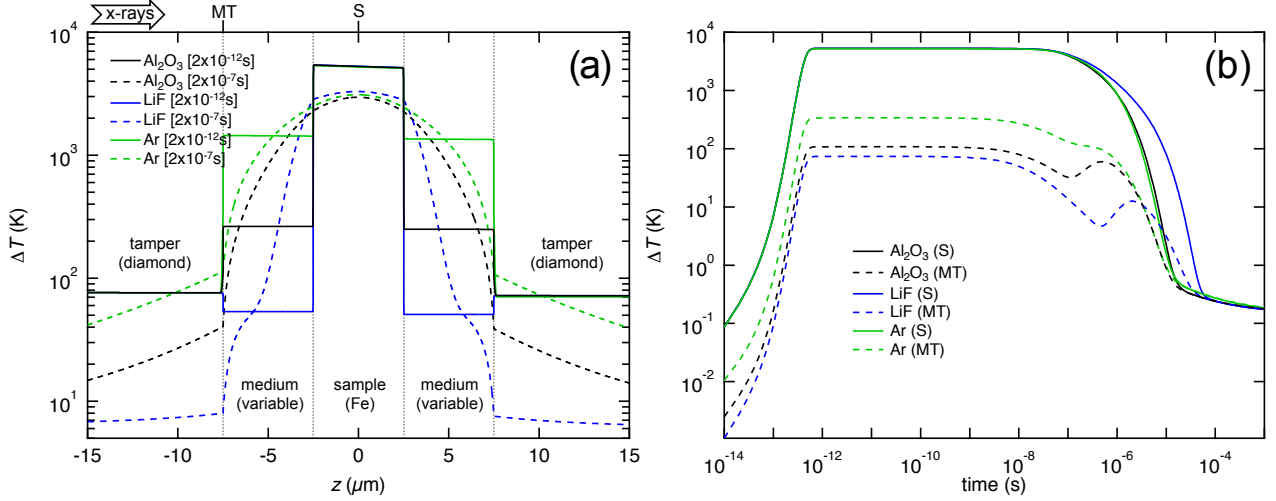


FIG. 9. Variance of thermal response with interfacial layer (medium) material. (a) Temperature change vs. position along the beam path center ($r = 0$) in the sample region. (b) Temperature change vs. time at sample center (S) and leading medium-tamper interface (MT). The black lines correspond to the standard simulation. Times are given in square brackets in seconds.

503 8. General features of target thermal evolution

504 Excluding the heat deposited by the x-ray irradiation, targets of the length scales de-
 505 scribed are effectively adiabatic on timescales up to 1-10 ns. As a consequence, considering
 506 irradiation on the timescales of typical FEL (10-100 fs) or synchrotron bunch (10-100 ps)
 507 sources, there should be little difference between peak temperature and subsequent thermal
 508 evolution, once LTE is achieved. Differences will appear only in the heating rate and poten-
 509 tially arise from nonlinear and ultrafast phenomena sensitive to this rate, but broadly, pulsed
 510 x-ray heating in the fs-ns range (Table I) will produce essentially similar target responses,
 511 since these timescales do not allow significant cooling during the energy deposition phase.
 512 Thus for fast sources, the principal parameter for assessing the temperature following x-ray
 513 illumination is the total pulse energy and its spatial distribution. Therefore the thermal
 514 evolution calculations made here are relevant for pulses of any length, up to the adiabatic
 515 limit of ~ 10 ns.

516 In these simulations interface temperatures between differentially heated surfaces are ef-
 517 fectively constant on shorter (adiabatic) timescales. Immediately after heating, the interface

518 achieves a temperature intermediate to that in the bulk of the contacting layers, defined in
 519 part by the bulk temperatures and in part by the layer thermal transport. These results are
 520 confirmed by the analytical solution for interfacial temperatures following rapid emplace-
 521 ment of an interfacial temperature discontinuity^{31,53}. For assumed constant layer thermal
 522 conductivities (Sec. II A 2), the interface temperature T_i is given as

$$523 \quad T_i = T_A + (T_B - T_A)/(1 + \sqrt{\kappa_A/\kappa_B}) \quad (18)$$

524 where subscripts indicate the contacting layers A and B. This closely predicts the simulated
 525 constant interface temperatures before cooling begins (after $\sim 10^{-8}$ s); e.g. in the baseline
 526 model at the leading interface between sample and medium, Eq. 18 predicts an initial
 527 interface temperature of ~ 3200 K, compatible with the modeled value (Fig. 2) of 3400 K.

528 For targets involving an additional low-Z (medium) layer between the sample and the
 529 tamper, a late rise in tamper temperature occurs as the heat wave from the high-Z sample
 530 reaches the tamper surface. The associated heating is often relatively minor, even where
 531 extreme sample temperatures are reached: e.g. for $\sim 55,000$ K in a Pb sample (Fig. 7) the
 532 heat pulse only raises the temperature at the tamper surface from ~ 400 to ~ 650 K. The
 533 timing and amplitude of the heat pulse is correlated with many properties of the system,
 534 showing, for example, a direct correlation with the thermal conduction properties of the
 535 materials. It can be observed that the arrival time of this pulse increases systematically
 536 with thermal diffusivity of the medium (Fig. 9 and Tables V and VI), i.e. it is fastest for
 537 a layer of dense argon ($\kappa = 1.9 \times 10^{-5}$ m²/s), slowest for LiF ($\kappa = 2.7 \times 10^{-6}$ m²/s), and
 538 intermediate for alumina ($\kappa = 1.5 \times 10^{-5}$ m²/s). The pulse amplitude is lowest for higher
 539 thermal conductivity tampers and highest for the insulating tamper (Fig. 8).

540 Comparison of the temperature at the sample center and near the interface between the
 541 sample and its surroundings provides some indication of the temperature gradient occurring
 542 in the sample. On shorter timescales the temperature distribution in the sample is defined
 543 exclusively by the absorption profile (Fig. 5) with an asymmetric gradient in initial tem-
 544 perature along the beampath (axial direction) possible in low keV experiments (Fig. 5) or
 545 when using high-Z samples (Fig. 7). With time, the sample temperature becomes more
 546 symmetric in the axial direction, regardless of the initial heating symmetry, with the lowest
 547 values near interfaces and the center remaining warmer.

548 For harder x-rays (15 keV and above), peak temperatures in the low-Z tamper are gen-

549 erally produced adjacent to the sample layers, either immediately upon heating (due to
550 interfacing with a hotter medium (Fig. 9) or sample (Fig. 6) layer, or after the heat wave
551 from the cooling sample reaches the tamper [Figs. 6(b), 7(b), 8(b)]. At lower keV, the
552 hottest portion of the tamper is the leading free surface due to efficient absorption of the
553 beam, however only at the lowest x-ray energy simulated (5 keV) is the tamper hotter than
554 the sample (indeed, there is negligible heating in the sample in this instance).

555 B. Hydrodynamic Model Results

556 A representative hydrodynamic model of the initial thermomechanical evolution of a
557 target after irradiation is shown in Fig. 10. Here a Mo sample, contained by an alumina
558 medium and diamond tamper (c.f. Fig. 7), is heated with 25 keV x-rays at $\sim 10^{15}$ W/cm²
559 for ~ 100 fs to peak temperature near 2×10^4 K.

560 Coincident with the heating, the sample layer experiences an increase in pressure to 55-70
561 GPa, whereas minor heating in the surrounding layers produces weaker initial pressurization.
562 Due to the differential heating and resulting differential pressures, waves of compression or
563 release emerge from interfaces between the heated layers². In this hydrodynamic model,
564 the hot, and hence high pressure sample layer undergoes release of pressure as it expands
565 and compresses the cold surrounding layers, driving them to higher pressure. The sample
566 expands beginning at its surfaces via an inward-moving release wave, while shock waves
567 are driven outward through the medium and toward the tamper. While this initial process
568 reduces the pressure in the sample, it is not to zero due to the presence of the medium and
569 the requirement of impedance matching at the sample-medium interface [Fig. 11(c)]. This
570 also requires the corresponding shock pressure to be some fraction of the initial thermal
571 pressurization.

572 The outward moving shocks reflect off the tampers and back toward the sample (at ~ 0.6
573 ns), producing a stress maximum on the tamper comparable in magnitude to the initial
574 thermal stress induced in the sample [Fig. 10(d)]. A more compressible medium reduces
575 this initial shock stress at the tamper for similar initial sample conditions. Meanwhile, the
576 inward moving release waves in the sample layer interact in the target center, producing
577 (beyond ~ 0.5 ns) a stress minimum in the sample which essentially restores the initial
578 (zero) pressure condition. These colliding release waves can also produce tensile stress in

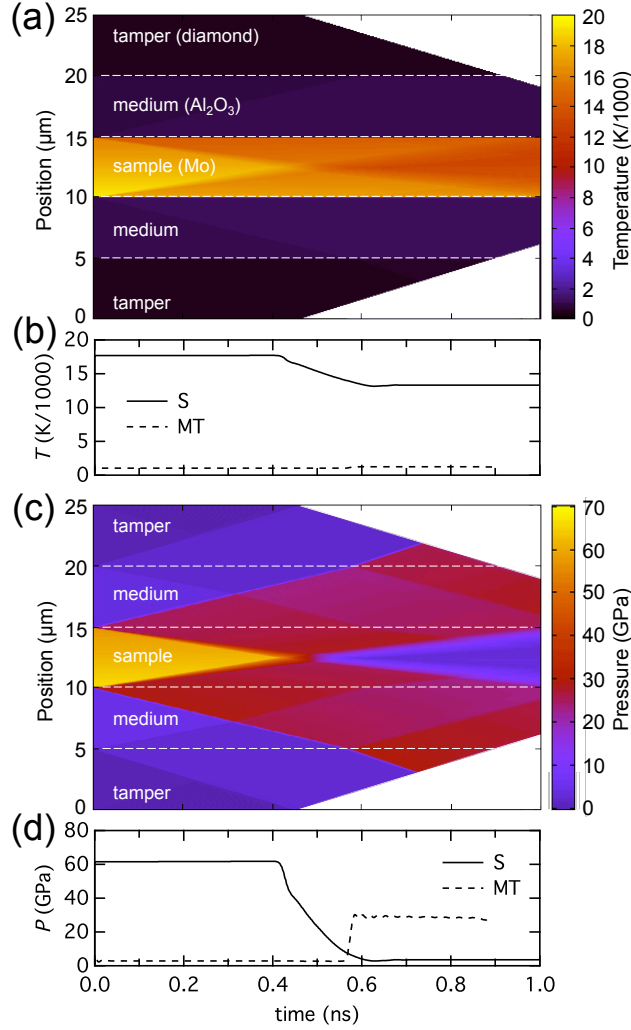


FIG. 10. One dimensional radiation hydrocode (HYADES) model for the sample area of a target in first 10^{-9} s after irradiation. Here a Mo sample ($5 \mu\text{m}$), surrounded by Al_2O_3 medium layers ($5 \mu\text{m}$) and diamond tampers (with thickness truncated to the displayed $5 \mu\text{m}$), is irradiated in a vacuum by 25 keV x-rays (see Fig. 7, dark blue curves, for a finite element model of a comparable system, at a different initial temperature). X-rays are incident from below. (a) Temperature throughout the simulated region (as a function of Lagrangian position and time). (b) temperature histories at the sample center (S) and medium-tamper interface (MT). Temperature changes are adiabatic in nature on this timescale. (c) Pressures throughout the simulated region and time domain. (d) pressure histories at the sample center and tamper surface. Regions where the simulation boundary interfered with the results were removed. The simulation makes a LTE approximation, which is suitable for treating these timescales⁵².

579 the target⁶ [Fig. 11(c)-(d)], which was seen in separate HYADES simulations if using suitable
 580 mechanical equations of state for the sample layer, and keeping peak stress sufficiently low.
 581 Compression and release is nearly symmetric about the sample center in Fig. 10, due to near-
 582 homogenous heating of each layer at 25 keV; strong asymmetry occurs for inhomogeneous
 583 heating in other simulations (e.g. if lower x-ray energy is used).

584 The hydrodynamic processes in target components of the current thicknesses are compa-
 585 rable in timescale to conventional shock experiments with durations of order nanoseconds,
 586 such as those produced by optical laser pulses^{1,13-17,32}. In such experiments, assuming condi-
 587 tions of thermodynamic equilibrium (i.e. in which materials follow an equilibrium equation
 588 of state) is a reasonable approximation. Simple thermodynamic calculations can predict
 589 essential details of the hydrodynamics, as captured in numerical models. For example, the
 590 magnitude of initial pressure can be considered an isochoric thermal pressure, after Eq. 16.
 591 For the 17700 K temperature rise in the Mo foil, having $K_T = 268$ GPa and $\beta = 1.50 \times 10^{-5}$
 592 K^{-1} , Eq. 16 gives $\Delta P_V \simeq 70$ GPa; this compares well with the ~ 62 GPa initial pressure
 593 rise calculated using HYADES (Fig. 10). Similarly, the timescale is sufficiently long that LTE
 594 conditions should be achieved⁵².

595 Dynamic stresses should largely relax in $\sim 10^{-9}$ s, before heat conduction initiates but
 596 with permanent and potentially significant effects on the temperature distribution in the
 597 target. Both shock (adiabatic) and release (isentropic) processes modify temperatures (Fig
 598 10A-B). The temperature in the medium and tamper are somewhat increased by shock,
 599 however more pronounced is the temperature reduction in the sample during its release.
 600 This expansion cooling can be described accurately with a thermodynamic model, taking
 601 an isentropic expansion (entropy S constant) of the Grüneisen form

$$602 \quad \gamma = - \left(\frac{\partial \ln T}{\partial \ln V} \right)_S, \quad (19)$$

603 where V is the specific volume. The Grüneisen parameter

$$604 \quad \gamma = \frac{\beta K_T V}{C_V}, \quad (20)$$

605 where C_V is the specific heat capacity at constant volume, is often found to follow the
 606 relationship

$$607 \quad \gamma = \gamma_0 \left(\frac{V}{V_0} \right)^q \quad (21)$$

608 where the subscript ‘0’ indicates reference (here ambient) conditions and the exponent q
609 is of order 1. Taking starting conditions of temperature and volume as T_0 and V_0 , initial
610 isochorically-heated equilibrium conditions T_1 and $V_1 = V_0$, and hydrodynamically-released
611 conditions T_2 and V_2 , and assuming constant thermal expansivity and complete release of
612 thermal pressure, we have

$$613 \quad V_2 = [\beta(T_2 - T_0) + 1] V_0, \quad (22)$$

614 i.e. the volume of the expanded state V_2 is equivalent to that produced on isobaric heating
615 to the same temperature. Taking $q = 1$ we obtain

$$616 \quad T_2 = T_1 \exp[-\gamma_0 \beta(T_2 - T_0)]. \quad (23)$$

617 Solving for an initial temperature $T_1 = 17700$ K in Mo, with $\gamma_0 = 1.51$ (taking $C_V = 3R$),
618 we obtain a release temperature of $T_2 = 13200$ K (a reduction of 25%), in agreement with
619 that calculated using HYADES for this initial condition (Fig. 10). While this can have a
620 potentially major effect on the starting temperature conditions for finite element models,
621 the expansion cooling becomes negligible at lower temperatures, i.e. for Mo at 1000 K the
622 expansion cooling is < 2 %.

623 As the inertial confinement time in such samples is in the range of picoseconds, radiation
624 pulses significantly longer than the picosecond level will not produce shock waves or large
625 pressure excursions, remaining at or close to the initial pressure.

626 IV. DISCUSSION

627 A. Pulse Train Response

628 Many high-power x-ray sources involve high-repetition-rate pulse trains, up to the MHz
629 level (pulse separations in the range of hundreds of ns, Table I), with even faster repeti-
630 tions possible using, e.g. split and delay lines or multiple RF-bucket filling⁵⁴. For sources
631 operating with high repetition rate, faster than the thermal relaxation time of samples (of
632 order $10 \mu\text{s}$ in these models), accumulation of thermal energy during a pulse train may oc-
633 cur. It may be crucial to consider this energy deposition for serial x-ray measurement (e.g.
634 crystallography⁵⁵) applications, even at lower power levels that may normally be considered
635 non-invasive. For example, considering the lowest level of irradiation studied here (0.0035

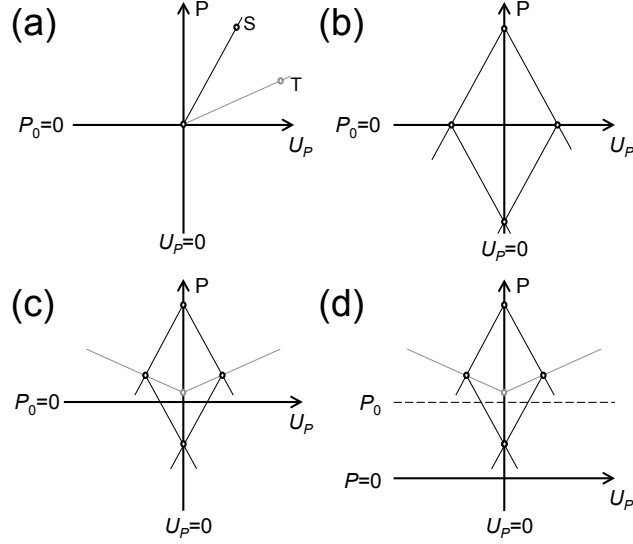


FIG. 11. Impedance match construction for the mechanical evolution of the x-ray heated sample (pressure P vs. mass velocity U_P). Material responses are lines, whereas dots are specific states achieved; S represents the sample and T a surrounding (i.e. tamper) material, presumed to be more weakly heated. Shocks and releases are approximated as linear elastic (i.e. $\Delta P \approx \rho c_S \Delta U_P$ where ρ is density and c_S is a wave velocity). Uniform heating in each layer is assumed. (a) Compression and release response of the high-Z sample (S) and a low-Z tamper (T), where the tamper is assumed to also have lower impedance. Lines indicate achievable states on compression from initial state $P_0 = 0$, $U_P = 0$; the dots represent particular compressed states. (b) Case of a freestanding sample layer in vacuum under x-ray heating. The sample foil is immediately driven to a high thermal pressure at zero velocity, and releases from both sides (Fig. 10), driving each side of the target to plus or minus a particle speed and zero pressure. These release waves converge at target center, causing a further stress reduction equivalent to the initial thermal pressure; i.e. the interacting release waves produce tension, and, if it exceeds of the tensile strength of the material, spall. (c) Case of a tamped sample, with only a partial reduction in pressure on initial release due to confinement by surrounding material (Fig. 10), and a reduced but not eliminated tension state (tension is prevented if sample and tamper have closer impedances). (d) While the preceding scenarios (a)-(c) apply for a typical laboratory condition with an initial pressure P_0 much less than the dynamic pressure (i.e. vacuum or ambient initial conditions), this scenario begins at a high initial hydrostatic pressure ($P_0 > 0$) comparable in magnitude to the dynamic pressure, as is made possible by pre-compression with a strong tamper^{32,48}. Achieved pressures are larger, while tension is suppressed.

636 mJ/pulse, Fig. 4) and assuming a pulse repetition rate of 4.5 MHz (220 ns between pulses,
637 taken from the bunch frequency of European XFEL, Table I), the temperature increase be-
638 tween pulses (including heating and cooling) is $\Delta T \simeq 30$ K, implying it would take roughly
639 50 pulses for an Fe sample to be driven in a step-wise fashion to its melting point (1811
640 K) from room temperature, in $\sim 11 \mu\text{s}$, assuming the temperature increases linearly with
641 time. As thermal pressures delivered during pulses have time to dissipate between pulses,
642 concomitant with thermal expansion, this type of heating can be thought of as being nearly
643 isobaric, though the transient thermal pressurization and expansion process itself may have
644 effects on the sample state (Sec. III B, Sec. IV B 3), while residual thermal pressure is
645 possible in well-confined samples⁴³.

646 A representative finite element model of the stepwise heating due to x-ray pulse trains for
647 the baseline experimental arrangement is shown in Fig. 12, using serial rather than single
648 exposures at the standard (0.35 mJ/pulse) fluence, assuming a repetition rate of 4.5 MHz.
649 The sample temperature grows in a sawtooth fashion, with each pulse producing a new
650 temperature peak followed by a gradual cooling until the next pulse. Cooling rates increase
651 with temperature, limiting achieved temperatures through a balance between heat added by
652 the x-ray pulses, and energy loss by conduction between pulses, such that peak temperatures
653 rise nonlinearly during the pulse train, and rapidly approach a limiting value. In this case
654 the temperature maximum is about three times greater than that achieved following a single
655 pulse. Similarly, at the lowest fluence (0.0035 mJ/pulse as used in the earlier estimate) the
656 sample would never reach melting, remaining below ~ 500 K in the limit.

657 Pulse train experiments may be useful for both probing and heating. For nominally non-
658 invasive probing applications, extending the duration between pulses can reduce the heat
659 accumulated in a fixed target, and ensure the sample temperature rise is minimized at the
660 time of each probing. On longer timescales, the sample temperature at the time of probing
661 is constant, so the data obtained can be treated as isothermal but at an elevated, satura-
662 tion temperature (after the initial pulses during which stabilization occurs). For deliberate
663 heating, minimizing pulse delay can increase the maximum achievable temperature, and
664 the functional length of the pulse train may be the number of pulses required to reach a
665 saturation value (e.g. ~ 15 pulses for a 4.5 MHz train, Fig. 12).

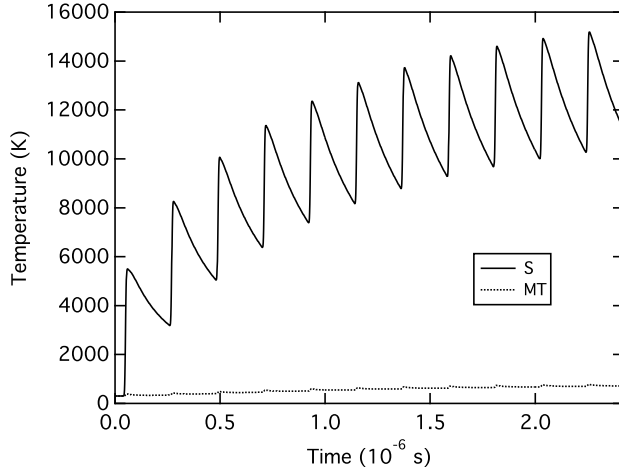


FIG. 12. Stepwise ‘isobaric’ heating by x-ray pulses delivered in a pulse train. The standard FE model configuration is used, with a 220 ns (4.5 MHz) pulse delay time assumed. Temperatures at the sample center (S) and medium-tamper interface (MT) are shown, for the first 11 pulses. Pulse duration is increased to a few ns in this model, to ensure numerical stability in the longer duration simulation.

666 B. Target Damage and Mitigation

667 Either in a single- or multiple-exposure experiment, the target lifetime can be of cen-
 668 tral importance. In a traditional isochoric heating experiment on thin layered targets, the
 669 lifetime is set by hydrodynamic expansion of the hot target, occurring as the ions gain en-
 670 ergy from electrons and expand into vapor. By confining the hot target in a tamper, this
 671 time can be increased. Use of very massive tampers surrounding a hotspot can lead to
 672 total confinement of even a dense plasma state, and reliable target survival^{20,23}. In what
 673 follows, basic mechanisms for target failure and their mitigation for long-duration and serial
 674 experiments are discussed. The considerations here apply principally to the effects of a sin-
 675 gle pulse, inasmuch as the primary damage should occur during the pulse and subsequent
 676 thermomechanical relaxation.

677 1. Thermal damage

678 Significant damage in targets can result from thermal effects, which include reversible
 679 and irreversible phase transformation (e.g. melting), reaction, strength reduction (i.e. in

680 the tamper), and for free surfaces, or at gaps, the possibility of vaporization. While some of
681 these effects are certain to occur in higher-Z (strongly heated) samples, the survival of the
682 target assembly will likely depend on tamper integrity. The temperature at the surfaces of
683 the tamper generally determine the peak temperatures to which the tampers are subject,
684 and thus the ability of tampers to survive the thermo-mechanical cycle and successfully
685 confine the sample throughout. This includes the tamper surfaces facing the sample, heated
686 by close contact with a hot sample layer, and the free surface facing the beam, heated by
687 peak fluence (Figs 2 – 10).

688 Many of the temperature conditions found in these simulations are in principal such that
689 the tampers can survive irradiation. Except for softer x-rays (Fig. 5), low-thermal conduc-
690 tivity tampers (Fig. 8) or no interfacial layer (Fig. 6), temperatures remain below probable
691 damage points of the tamper in these experiments even for significant heating in the sample
692 layer (by 10^3 - 10^4 K). For the high-thermal conductivity tampers, the tamper temperature
693 remains below graphitization and oxidation points for diamond (~ 1000 - 2000 K), the sub-
694 limation point for graphite (~ 4000 K) and melting points for Be and Al_2O_3 (~ 1500 - 2300
695 K), for 25 keV radiation (Fig. 8). For the standard experimental configuration (diamond-
696 alumina-iron and 25 keV x-rays), the tamper begins with only about $\sim 2\%$ of the temper-
697 ature change in the sample (Fig 4) and never exceeds this as the target cools. Even for
698 temperatures exceeding 50,000 K in any sample, diamond tamper temperatures need not
699 exceed 600 -1400 K (Figs 4 and 7), low enough to prevent thermal damage, particularly for
700 brief heating. In contrast, the low thermal conductivity plastic tamper (Fig. 8) leads to
701 elevated thermal confinement near the tamper interface with the sample region, and heating
702 of the tamper surface up to ~ 1200 K for a sample temperature of ~ 6000 K, well beyond the
703 thermal degradation point of the material (~ 670 K for Kapton).

704 **2. Radiation damage**

705 Ultrahigh intensity laser sources can have substantial direct influence on materials in-
706 cluding radiative damage and electronic excitation: insulators can be rapidly and transiently
707 transformed to metals⁵⁶, bonds can be disrupted⁹, and structural transformations that nor-
708 mally would be sluggish can occur instantaneously⁴⁰. Such ‘non-thermal’ radiation effects
709 can be quantified by the amount of energy absorbed per atom, Q_{atom} . From Eq. 4, in-

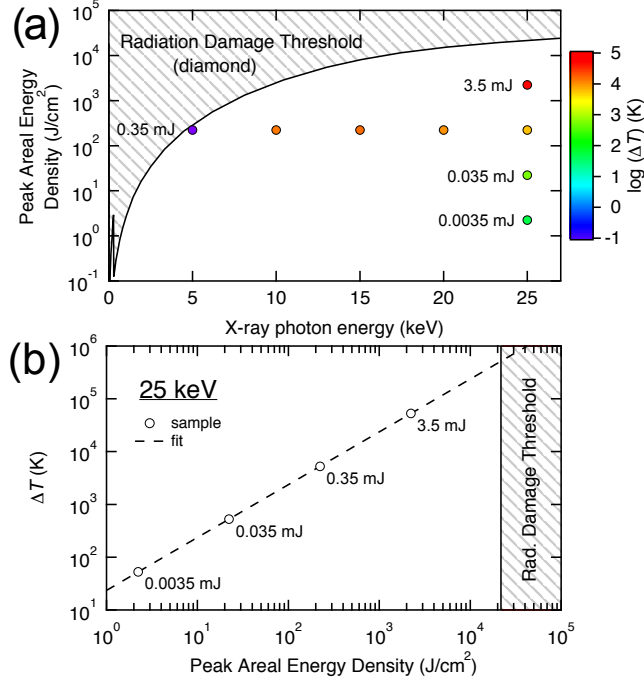


FIG. 13. Comparison of simulated conditions in standard targets (diamond tamper, Al_2O_3 medium, iron sample) with the ‘nonthermal’ radiative damage threshold predicted for diamond⁴⁰, given in terms of peak areal energy density Λ_{max} . (a) Radiation damage threshold of diamond compared with simulated conditions of x-ray energy (Fig. 5) and fluence (Fig. 4); color indicates peak temperature achieved in the sample. (b) Achieved sample temperature as a function of fluence at 25 keV. Total energy per pulse is given in mJ.

710 tegrating over the pulse, and ignoring beam attenuations, the maximum of this quantity
 711 is

$$712 \quad Q_{atom} = \frac{\Lambda_{max} \alpha A}{\rho} \quad (24)$$

713 where A is atomic mass (Eq. 14) and peak energy density per area is Λ_{max} (Eq. 11). Use
 714 of this criterion then leads to rough constraints on acceptable irradiation conditions.

715 Considering again tamper integrity, direct radiative ablation is possible at free surfaces
 716 where unconfined atoms may easily escape the target, at $Q_{atom} \sim 1$ eV; however, for the low-Z
 717 tampers considered here, such as Be and C polymorphs, this limit is not easily reached⁴⁵. For
 718 diamond, nonthermal breakdown of diamond to graphite occurs at relatively lower absorbed
 719 energy, ~ 0.7 eV/atom^{40,45}. Even with this more conservative criterion, modeled irradiation
 720 conditions remain below the nonthermal damage threshold for diamond⁴⁰ [Fig. 13(a)] except

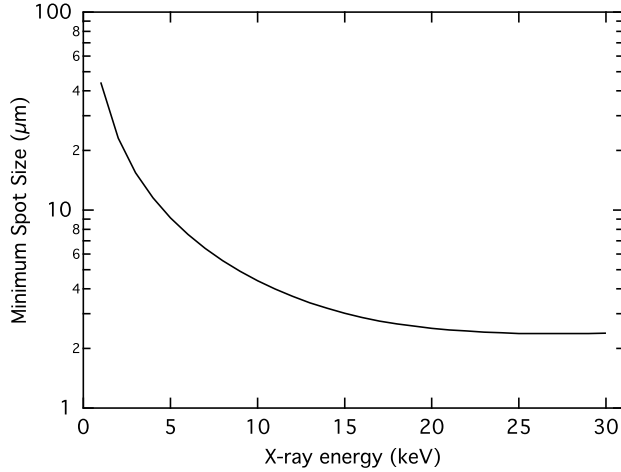


FIG. 14. Effective beam diameter lower limit in diamond assuming a damage threshold of 0.7 eV/atom (graphitization limit^{40,45}) and $N = 3.5 \times 10^{11}$ photons per pulse (0.06-1.7 mJ/pulse for 1-30 keV). For the beam diameter used in these simulations, $\sim 12 \mu\text{m}$, the damage threshold is exceeded below 5 keV (see also Fig. 13) but is within tolerance at higher x-ray energies.

721 possibly at the lowest x-ray energy (5 keV) where, due to considerable direct heating from
 722 the x-ray beam (Fig. 5), the overall damage threshold is likely to be at even lower fluence.
 723 At 25 keV [Fig. 13(b)], a diamond tamper could survive irradiation up to iron sample
 724 temperatures of ~ 40 eV ($\sim 5 \times 10^5$ K), and higher-Z sample temperatures in the 100 eV
 725 range (c.f. Fig. 7); tamper damage risk from heating and shock is likely to be more critical at
 726 such conditions. In summary, direct radiation damage may not be a major factor in target
 727 survival and performance. An effective lower limit on beam diameter to avoid radiation
 728 damage in diamond is given in Fig. 14.

729 **3. Thermo-mechanical damage**

730 With the rapid, bulk heating of samples occurring faster than pressure wave propagation
 731 in our simulations (i.e. $\sigma_t \ll d_S/c$), thermal pressure develops as a consequence of heating.
 732 The large mechanical stresses associated with target heating can introduce immediate or
 733 cumulative damage to targets, including irreversible deformations, flow, fracturing, delami-
 734 nation at interfaces, and spall. Thus, target survival after a single pulse or series of pulses
 735 will depend on the integrity of the target under mechanical stresses as temperature and
 736 pressure are raised, and as pressures dissipate hydrodynamically as stress differentials relax

737 (Fig. 10). The system can exhibit a complex thermomechanical evolution as it moves to-
738 ward equilibrium if surrounding tampers are sufficiently strong to resist free hydrodynamic
739 expansion. Mechanical stresses could act in conjunction with direct thermal effects including
740 softening, melting, and vaporization to promote damage.

741 The magnitudes of mechanical stress initially generated in the target (Eq. 16) will be
742 similar to those associated with subsequent pressure waves. In the present examples, while
743 this value can be large, relatively lower stress is applied to the surrounding materials and
744 tampers due to impedance matching requirements. In our example, for the ~ 60 GPa initial
745 stress in the Mo sample, shock waves forming in conjunction with the release of the hot
746 sample layer and striking (and reverberating from) the tamper (diamond in this instance)
747 are ~ 30 GPa in amplitude (Fig. 10). While tamper temperature is increased somewhat
748 by this shock, in terms of damage threshold it is the pressure perturbation that will likely
749 cause the immediate (mechanical) damage. Notably, the diamond tamper in this case can
750 withstand the shock wave (which falls below the dynamic yielding point¹³) as well as the
751 subsequent heat wave (Fig. 7). However, shock waves of this amplitude could severely
752 damage other tampers. As the pressure medium controls the shock amplitude, softer media
753 could be used to minimize the shock stress, while complete suppression of shock could be
754 achieved using pulses with durations exceeding the hydrodynamic relaxation times (e.g.
755 synchrotron bunch pulses, Table I).

756 C. Anvil Cell Configuration

757 As the target configuration discussed here is broadly identical to that of static high
758 pressure cells, this application is considered in detail below. In an anvil cell type design, the
759 sample is configured to withstand high stresses in the sample area via confinement by thick,
760 hard materials. Diamond anvils provide unmatched capabilities for pressure application and
761 resistance, for up to ~ 1000 GPa⁵⁰, while other strong, low-Z candidates for high-strength
762 tamper-anvils include sapphire (single crystal Al_2O_3) and Moissanite (SiC)⁴¹.

763 The prior considerations for limiting target damage suggest that improving sample con-
764 finement, i.e. using a pressure cell configuration, could enhance target stability and survival.
765 In this configuration, thermal expansion of the hot sample is limited⁴³ ensuring the material
766 remains at or near its initial density regardless of heating. Cracks or voids which can be

767 present in multilayer target assemblies or ordinarily develop due to thermal stresses can
768 be suppressed. The ability of anvil cells to resist the heating and associated mechanical
769 stresses in hot samples have long been demonstrated using infrared lasers to heat samples,
770 to temperatures in the range of several eV, over timescales of microseconds and longer^{18,20,43}.
771 With similar conditions of temperature, pressure, and timescale found in the present x-ray
772 heating simulations, many advantages and techniques of the anvil cell configuration may be
773 useful in thickly-tamped target experiments generally.

774 In one possible experiment, a tamped sample could be placed under some small initial
775 stress (to ensure good initial confinement, and void elimination). Thermal stresses intro-
776 duced by x-ray heating could be controlled by the anvil's high strength and potential stress
777 resistance. So long as the anvils can withstand the additional mechanical stresses (on the
778 order of GPa or higher for conditions considered here, Sec. IIIB) and any heating (Sec.
779 III A), the target could be stabilized indefinitely. The anvil cell provides a built in way to
780 safely relieve thermal stresses in samples to a mechanical equilibrium confinement state⁴³
781 without hydrodynamic expansion, solving a principal issue in tamped laser-driven targets
782 that may only be partially mitigated by tamping alone. The extended target stabiliza-
783 tion would permit studies over a wide range of timescales, accessing phenomena including
784 electron-ion thermalization, structural transitions and thermal conduction, and enable re-
785 peated exposures of the same sample on arbitrary timescales, and sample recovery. This
786 approach would require some apparatus to apply a compressive force across the target, as in
787 a standard pressure cell configuration, with suitable windows for admittance and observation
788 of radiation.

789 The ability to pre-compress samples to elevated densities can also provide, in conjunc-
790 tion with x-ray irradiation, a route to studying laser-plasma interactions and warm dense
791 matter at conditions of very high density, exceeding that of conventional solid states. Static
792 pre-compression of matter to hundreds of GPa confining pressure, or larger using mod-
793 ern double-stage anvils⁵⁰, is a widely used method, compatible with a variety of strategies
794 to further modulate sample conditions (e.g. temperature) and probe sample properties at
795 extremes. Our models demonstrate that coupling a high density sample with intense x-ray ir-
796 radiation on modern light sources can offer a new approach for exploring ultra-dense and hot
797 states, complementary with dynamic compression and traditional optical-laser-heated DAC,
798 in terms of achievable pressure-temperature-timescale conditions. Indeed, x-ray heating may

799 serve as an alternative to optical laser-heating^{18,20,41,43} of anvil cells, with the modeled pulsed
800 x-ray heating of samples closely resembling pulsed optical laser heating approaches¹⁸⁻²¹, with
801 several key differences. Optical heating techniques produce large temperature gradients in
802 samples, i.e. where heat must conduct from a heated surface, and are susceptible to un-
803 predictable coupling related to surface or sample properties; furthermore probes must be
804 carefully aligned with the heated spots. Hard x-ray heating can in contrast provide ho-
805 mogenous temperatures in the sample bulk on rapid timescales²⁷, simple coupling with the
806 sample, and automatic alignment of heating and x-ray probe beams. X-ray heating may be
807 particularly useful where introduction of optical laser energy to samples is impractical or
808 impossible, such as where optically opaque anvils are used, e.g. in double-stage anvil⁵⁰ or
809 multi-anvil applications, where the optical damage threshold of anvils may be exceeded in
810 high-energy applications³², or where nominally transparent insulating media transform to
811 opaque conductors during heating²⁰.

812 Addition of pressure could, at least for the sample interfacing region, serve to elevate
813 the damage thresholds for a diamond tamper, both in terms of its thermal resistance and
814 mechanical resistance. Thermal graphitization is prevented above ~ 13 GPa where diamond
815 becomes the stable structure of carbon, whereas the melting temperature of diamond at these
816 conditions exceeds 4000 K¹⁶. Confining pressure also increases the strength of diamond¹³, a
817 fact employed in modern anvil cell designs to enhance the potential stress resistance⁵⁰.

818 Fig. 15 compares two different types of geometry used in our simulations: the first is
819 the cylindrical geometry used in the main simulations, and the second is a representation of
820 an anvil cell. For similar peak temperatures, there is little difference between the simplified
821 cylindrical model and the more complete model in terms of the temperature evolution of the
822 sample area. Thus finite-element calculations using the present simple geometry accurately
823 describe the anvil cell design.

824 V. CONCLUSIONS

825 This study describes the thermo-mechanical response of macroscale targets subjected to
826 irradiation by intense, brief x-ray pulses, similar to those now produced by the current gen-
827 eration of x-ray free electron lasers. These targets use thick, light-element tamper or anvil
828 layers, which are transparent at hard x-ray energies, to confine a thin target assembly, com-

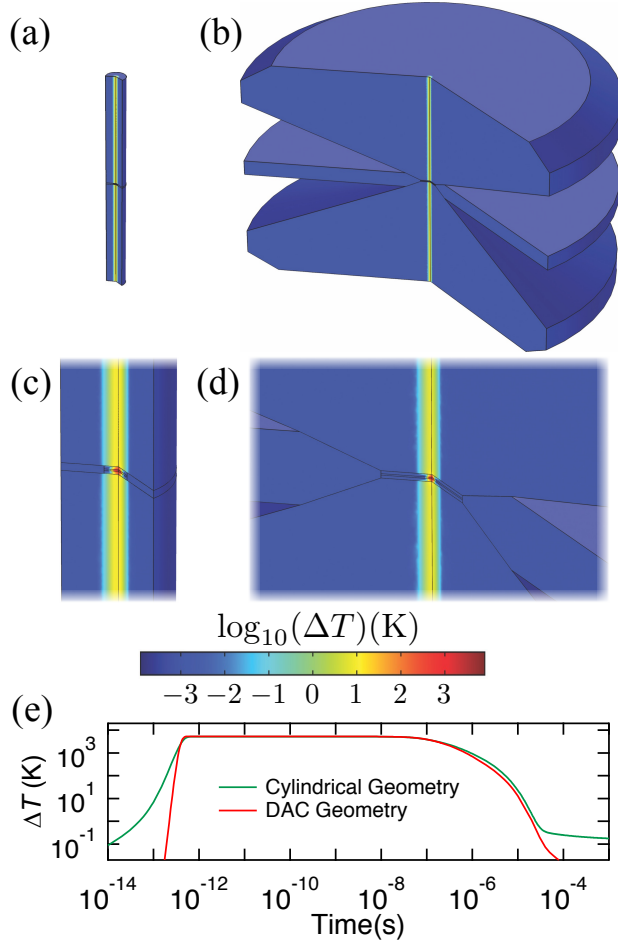


FIG. 15. Comparison between temperature distributions for the main simulation geometry with the standard materials (a) and a comparable simulation for a diamond anvil cell (b). The time of the simulation snapshots in (a)-(d) is 1×10^{-7} s. Close-ups of sample regions (c)-(d) show nearly identical temperature behavior at these early times. A comparison of the temperature history at the sample center shows notable differences in simulated temperature only during heating (a shorter pulse was assumed for the DAC simulation), and very late in the cooling phase. The latter difference is due to the larger heat sink provided by the full-size target assembly, resulting in lower limiting temperature.

829 prising one or more layers which may be strongly absorbing to x-ray radiation. The thermal
 830 and mechanical evolution of the x-ray heated target after the rapid deposition of heat is
 831 treated using finite-element and radiation-hydrodynamics calculations. We find that con-
 832 ventional hydrodynamics, classical diffusive heat transfer, and equilibrium thermodynamics
 833 can accurately treat the principal thermo-mechanical phenomena for the length and time

834 scales characteristic of such large targets.

835 Conditions achieved in the most extreme experiments simulated fall within the regime of
836 warm dense matter, i.e. conditions near or above solid density and temperatures exceeding
837 several eV, where ratios of Coulomb interaction energy to thermal kinetic energy Γ (the
838 coupling parameter) and of Fermi energy to thermal energy Θ (the degeneracy parameter)
839 approach unity. That these conditions could be sustained for up to microsecond timescales
840 using suitable target configurations offers a potential way to study properties of warm dense
841 matter under total thermodynamic equilibrium conditions, on timescales exceeding those
842 of modern experiments that use laser-driven shock waves or unconfined isochoric heating.
843 Using thick tampers to apply initial pressure on samples and taking advantage of serial
844 irradiation can enable further exploration of novel regimes of density, temperature, and
845 timescale in warm dense matter. Target survival over one or more exposures is controlled
846 by targets' potential resistance to temperatures on the order of an eV (thousands of degrees
847 Kelvin), mechanical stress close to one million atmospheres (100 GPa), and radiation levels
848 close to damage thresholds, all found to be survivable depending on target design.

849 For thick targets of the considered design (μm -thick samples with mm-thick tampers),
850 the thermal response due to intense x-ray illumination should be similar at different facilities
851 offering sub-nanosecond pulses, including modern free electron laser and synchrotron sources.
852 Due to the thermal inertia of samples of this scale, temperatures achieved and cooling
853 behavior are not strongly dependent on pulse lengths, but on total energy dose. Thus modern
854 synchrotron sources with ~ 100 ps pulse duration may produce a similar level of heating to
855 that at an XFEL with ~ 100 fs pulses, for equivalent pulse energy. Heat accumulation over
856 pulse trains with MHz repetition rates characteristic of such facilities can lead to further
857 temperature rise, though this effect is somewhat mitigated by equilibrium between heating
858 and cooling that leads to effectively isothermal experiments on longer timescales. Thus,
859 consideration of x-ray heating effects may be necessary even in nominally non-invasive x-
860 ray measurements at many modern, high brightness, high repetition-rate x-ray sources,
861 including synchrotron facilities. Certain related processes could be more sensitive to the
862 radiation intensity and pulse duration, including shock-wave generation, which would occur
863 under 100-fs XFEL but not 100-ps synchrotron irradiation.

864 The multilayer target configuration discussed here is informed by, and mimics, the con-
865 figuration of a static high pressure anvil system, of which the diamond-anvil cell uniaxial

866 press is the most relevant. Anvil cells have the ability of preparing initial states of elevated
867 density and pressure in samples, including different structural states, prior to excitation to
868 more extreme states; their wide use in preparing samples for shock-wave compression^{32,48}
869 and near-isochoric optical laser heating^{18,20,43} experiments suggests many possibilities for
870 accessing otherwise unreachable states of matter with x-ray heating, and for enabling diag-
871 nosis of these states by a wide range of radiation types. While experience with conventional
872 optical laser heating of anvil cells is relevant, x-ray heating has the potential to bring new ad-
873 vantages for heating pre-compressed matter, including direct volumetric heating, automatic
874 x-ray probe alignment with heated areas, and insensitivity to target optical thresholds. The
875 confinement afforded through an anvil cell design is another way to stabilize tamped targets
876 against thermomechanical stress generally and extend experimental lifetimes by limiting
877 them with conductive rather than hydrodynamic dissipation, and ensure target survival for
878 continued exposure and recovery of samples from extremes.

879 Ultimately experiments must be performed to assess the accuracy of the models devel-
880 oped here, as are currently possible at modern x-ray sources. Further improvements in these
881 models will likely be required to compare with experiments, including coupling of ther-
882 momechanical and thermal conductive processes and more accurate treatment of radiation
883 coupling in the sample, which are likely to be essential at higher radiation intensities.

884 **ACKNOWLEDGEMENTS**

885 Thanks to Y. Ping for providing HYADES code, and J. Wark, U. Zastrau, S. Pascarelli,
886 V. Lyamanev, C. Strohm, S. Toleikis, J. Eggert and two anonymous reviewers for help-
887 ful discussions and suggestions for improving the manuscript. This work was supported
888 by Grants EP/P024513/1 and EP/R02927X/1 from the U.K. Engineering and Physical
889 Sciences Research Council (EPSRC), CONACyT and UAEMéx, Leverhulme Trust grant
890 RPG-2017-035, and Grant No. 4070200747 Fel from the U.K. Science and Technology
891 Funding Council (STFC). This work was performed in part under the auspices of the U.S.
892 Department of Energy by Lawrence Livermore National Laboratory under Contract No.
893 DE-AC52-07NA27344.

894 **REFERENCES**

- 895 ¹A. Ng, T. Ao, F. Perrot, M. Dharma-Wardana, and M. Foord, *Laser and Particle Beams*
896 **23**, 527 (2005).
- 897 ²Y. Sentoku, A. J. Kemp, R. Presura, M. S. Bakeman, and T. E. Cowan, *Physics of*
898 *Plasmas* **14**, 122701 (2007).
- 899 ³L. B. Fletcher, H. J. Lee, B. Barbreil, M. Gauthier, E. Galtier, B. Nagler, T. Döppner,
900 S. LePape, T. Ma, A. Pak, D. Turnbull, T. White, G. Gregori, M. Wei, R. W. Falcone,
901 P. Heimann, U. Zastra, J. B. Hastings, and S. H. Glenzer, *Review of Scientific Instru-*
902 *ments* **85**, 11E702 (2014).
- 903 ⁴P. K. Patel, A. J. Mackinnon, M. H. Key, T. E. Cowan, M. E. Foord, M. Allen, D. F.
904 Price, H. Ruhl, P. T. Springer, and R. Stephens, *Phys. Rev. Lett.* **91**, 125004 (2003).
- 905 ⁵G. Gregori, S. B. Hansen, R. Clarke, R. Heathcote, M. H. Key, J. King, R. I. Klein,
906 N. Izumi, A. J. Mackinnon, S. J. Moon, H. Park, J. Pasley, N. Patel, P. K. Patel, B. A.
907 Remington, D. D. Ryutov, R. Shepherd, R. A. Snavely, S. C. Wilks, B. B. Zhang, and
908 S. H. Glenzer, *Contributions to Plasma Physics* **45**, 284 (2005).
- 909 ⁶D. S. Ivanov and L. V. Zhigilei, *Phys. Rev. B* **68**, 064114 (2003).
- 910 ⁷A. Lévy, P. Audebert, R. Shepherd, J. Dunn, M. Cammarata, O. Ciricosta, F. Deneuille,
911 F. Dorchies, M. Fajardo, C. Fourment, D. Fritz, J. Fuchs, J. Gaudin, M. Gauthier, A. Graf,
912 H. J. Lee, H. Lemke, B. Nagler, J. Park, O. Peyrusse, A. B. Steel, S. M. Vinko, J. S. Wark,
913 G. O. Williams, D. Zhu, and R. W. Lee, *Physics of Plasmas* **22**, 030703 (2015).
- 914 ⁸T. G. White, N. J. Hartley, B. Borm, B. J. B. Crowley, J. W. O. Harris, D. C. Hochhaus,
915 T. Kaempfer, K. Li, P. Neumayer, L. K. Pattison, F. Pfeifer, S. Richardson, A. P. L.
916 Robinson, I. Uschmann, and G. Gregori, *Phys. Rev. Lett.* **112**, 145005 (2014).
- 917 ⁹U. Zastra, P. Sperling, A. Becker, T. Bornath, R. Bredow, T. Döppner, S. Dzyarzhyski,
918 T. Fennel, L. B. Fletcher, E. Förster, C. Fortmann, S. H. Glenzer, S. Göde, G. Gre-
919 gori, M. Harmand, V. Hilbert, B. Holst, T. Laarmann, H. J. Lee, T. Ma, J. P. Mithen,
920 R. Mitzner, C. D. Murphy, M. Nakatsutsumi, P. Neumayer, A. Przystawik, S. Roling,
921 M. Schulz, B. Siemer, S. Skruszewicz, J. Tiggesbäumker, S. Toleikis, T. Tschentscher,
922 T. White, M. Wöstmann, H. Zacharias, and R. Redmer, *Phys. Rev. E* **90**, 013104 (2014).
- 923 ¹⁰A. N. Mostovych and Y. Chan, *Phys. Rev. Lett.* **79**, 5094 (1997).

- 924 ¹¹Y. Ping, A. Fernandez-Panella, H. Sio, A. Correa, R. Shepherd, O. Landen, R. A. London,
925 P. A. Sterne, H. D. Whitley, D. Fratanduono, T. R. Boehly, and G. W. Collins, *Physics*
926 *of Plasmas* **22**, 092701 (2015).
- 927 ¹²N. A. Tahir, I. V. Lomonosov, B. Borm, A. R. Piriz, A. Shutov, P. Neumayer, V. Bagnoud,
928 and S. A. Piriz, *The Astrophysical Journal Supplement Series* **232**, 1 (2017).
- 929 ¹³R. S. McWilliams, J. H. Eggert, D. G. Hicks, D. K. Bradley, P. M. Celliers, D. K. Spaulding,
930 T. R. Boehly, G. W. Collins, and R. Jeanloz, *Phys. Rev. B* **81**, 014111 (2010).
- 931 ¹⁴D. Kraus, J. Vorberger, A. Pak, N. J. Hartley, L. B. Fletcher, S. Frydrych, E. Galtier, E. J.
932 Gamboa, D. O. Gericke, S. Glenzer, E. Granados, M. J. MacDonald, A. J. MacKinnon,
933 E. E. McBride, I. Nam, P. Neumayer, M. Roth, A. M. Saunders, A. K. Schuster, P. Sun,
934 T. van Driel, T. Döppner, and R. W. Falcone, *Nature Astronomy* **1**, 606 (2017).
- 935 ¹⁵K. Falk, M. Holec, C. J. Fontes, C. L. Fryer, C. W. Greeff, H. M. Johns, D. S. Montgomery,
936 D. W. Schmidt, and M. Šmíd, *Phys. Rev. Lett.* **120**, 025002 (2018).
- 937 ¹⁶J. H. Eggert, D. G. Hicks, P. M. Celliers, D. K. Bradley, R. S. McWilliams, R. Jeanloz,
938 J. E. Miller, T. R. Boehly, and G. W. Collins, *Nat Phys* **6**, 40 (2010).
- 939 ¹⁷M. G. Gorman, R. Briggs, E. E. McBride, A. Higginbotham, B. Arnold, J. H. Eggert, D. E.
940 Fratanduono, E. Galtier, A. E. Lazicki, H. J. Lee, H. P. Liermann, B. Nagler, A. Rothkirch,
941 R. F. Smith, D. C. Swift, G. W. Collins, J. S. Wark, and M. I. McMahon, *Phys. Rev.*
942 *Lett.* **115**, 095701 (2015).
- 943 ¹⁸A. F. Goncharov, V. B. Prakapenka, V. V. Struzhkin, I. Kantor, M. L. Rivers, and D. A.
944 Dalton, *Review of Scientific Instruments* **81**, 113902 (2010).
- 945 ¹⁹A. F. Goncharov, M. Wong, D. Allen Dalton, J. G. O. Ojwang, V. V. Struzhkin,
946 Z. Konôpková, and P. Lazor, *Journal of Applied Physics* **111**, 112609 (2012).
- 947 ²⁰R. McWilliams, D. A. Dalton, Z. Konôpková, M. F. Mahmood, and A. F. Goncharov,
948 *Proceedings of the National Academy of Sciences* **112**, 7925 (2015).
- 949 ²¹Z. Konôpková, R. S. McWilliams, N. Gomez-Perez, and A. F. Goncharov, *Nature* **534**,
950 99 (2016).
- 951 ²²Y. Ping, D. Hanson, I. Koslow, T. Ogitsu, D. Prendergast, E. Schwegler, G. Collins, and
952 A. Ng, *Phys. Rev. Lett.* **96**, 255003 (2006).
- 953 ²³A. Vailionis, E. G. Gamaly, V. Mizeikis, W. Yang, A. V. Rode, and S. Juodkazis, *Nat*
954 *Commun* **2**, 445 (2011).

- 955 ²⁴S. L. Johnson, P. A. Heimann, A. G. MacPhee, A. M. Lindenberg, O. R. Monteiro,
956 Z. Chang, R. W. Lee, and R. W. Falcone, *Phys. Rev. Lett.* **94**, 057407 (2005).
- 957 ²⁵J. Bailey, P. Arnault, T. Blenski, G. Dejonghe, O. Peyrusse, J. MacFarlane, R. Mancini,
958 M. Cuneo, D. Nielsen, and G. Rochau, *Journal of Quantitative Spectroscopy and Radiative*
959 *Transfer* **81**, 31 (2003).
- 960 ²⁶U. Zastra, C. Fortmann, R. R. Fäustlin, L. F. Cao, T. Döppner, S. Düsterer, S. H.
961 Glenzer, G. Gregori, T. Laarmann, H. J. Lee, A. Przystawik, P. Radcliffe, H. Reinholz,
962 G. Röpke, R. Thiele, J. Tiggesbäumker, N. X. Truong, S. Toleikis, I. Uschmann, A. Wier-
963 ling, T. Tschentscher, E. Förster, and R. Redmer, *Phys. Rev. E* **78**, 066406 (2008).
- 964 ²⁷B. Nagler, U. Zastra, R. R. Faustlin, S. M. Vinko, T. Whitcher, A. J. Nelson, R. Sobiera-
965 jski, J. Krzywinski, J. Chalupsky, E. Abreu, S. Bajt, T. Bornath, T. Burian, H. Chapman,
966 J. Cihelka, T. Döppner, S. Dusterer, T. Dezelzainis, M. Fajardo, E. Forster, C. Fortmann,
967 E. Galtier, S. H. Glenzer, S. Gode, G. Gregori, V. Hajkova, P. Heimann, L. Juha, M. Jurek,
968 F. Y. Khattak, A. R. Khorsand, D. Klinger, M. Kozlova, T. Laarmann, H. J. Lee, R. W.
969 Lee, K.-H. Meiwes-Broer, P. Mercere, W. J. Murphy, A. Przystawik, R. Redmer, H. Rein-
970 holz, D. Riley, G. Roppke, F. Rosmej, K. Saksl, R. Schott, R. Thiele, J. Tiggesbaumker,
971 S. Toleikis, T. Tschentscher, I. Uschmann, H. J. Vollmer, and J. S. Wark, *Nature Physics*
972 **5**, 693 (2009).
- 973 ²⁸S. M. Vinko, O. Ciricosta, B. I. Cho, K. Engelhorn, H. K. Chung, C. R. D. Brown,
974 T. Burian, J. Chalupsky, R. W. Falcone, C. Graves, V. Hajkova, A. Higginbotham, L. Juha,
975 J. Krzywinski, H. J. Lee, M. Messerschmidt, C. D. Murphy, Y. Ping, A. Scherz, W. Schlot-
976 ter, S. Toleikis, J. J. Turner, L. Vysin, T. Wang, B. Wu, U. Zastra, D. Zhu, R. W. Lee,
977 P. A. Heimann, B. Nagler, and J. S. Wark, *Nature* **482**, 59 (2012).
- 978 ²⁹S. H. Glenzer, L. B. Fletcher, E. Galtier, B. Nagler, R. Alonso-Mori, B. Barbrel, S. B.
979 Brown, D. A. Chapman, Z. Chen, C. B. Curry, F. Fiuza, E. Gamboa, M. Gauthier, D. O.
980 Gericke, A. Gleason, S. Goede, E. Granados, P. Heimann, J. Kim, D. Kraus, M. J. Mac-
981 Donald, A. J. Mackinnon, R. Mishra, A. Ravasio, C. Roedel, P. Sperling, W. Schumaker,
982 Y. Y. Tsui, J. Vorberger, U. Zastra, A. Fry, W. E. White, J. B. Hasting, and H. J. Lee,
983 *Journal of Physics B: Atomic, Molecular and Optical Physics* **49**, 092001 (2016).
- 984 ³⁰A. M. Saunders, B. Lahmann, G. Sutcliffe, J. A. Frenje, R. W. Falcone, and T. Döppner,
985 *Phys. Rev. E* **98**, 063206 (2018).

986 ³¹R. G. McQueen and D. G. Isaak, *Journal of Geophysical Research-Solid Earth and Planets*
987 **95**, 21753 (1990).

988 ³²M. R. Armstrong, J. C. Crowhurst, S. Bastea, and J. M. Zaug, *Journal of Applied Physics*
989 **108**, 023511 (2010).

990 ³³Linac Coherent Light Source, “MEC Specifications,” (2017), <https://lcls.slac.stanford.edu/instruments/mec/specifications>, Last accessed 07-2018.

992 ³⁴“LCLS-II final design report, rep. LCLSII-1.1-DR-0251,” Tech. Rep. (SLAC, Menlo Park,
993 USA, 2015).

994 ³⁵T. Raubenheimer, in *Proc. 60th ICFA Advanced Beam Dynamics Workshop (FLS’18),*
995 *Shanghai, China, 5-9 March 2018*, ICFA Advanced Beam Dynamics Workshop No. 60
996 (JACoW Publishing, Geneva, Switzerland, 2018) pp. 6–11.

997 ³⁶M. Yabashi, H. Tanaka, and T. Ishikawa, *Journal of Synchrotron Radiation* **22**, 477 (2015).

998 ³⁷G. Garbarino, “Id27, an advanced high flux XRD beamline for science under extreme con-
999 ditions: present and future,” (2017), presentation at the 55th EHPRG Meeting, Poznań,
1000 Poland.

1001 ³⁸P. M. Celliers, M. Millot, S. Brygoo, R. S. McWilliams, D. E. Fratanduono, J. R. Rygg,
1002 A. F. Goncharov, P. Loubeyre, J. H. Eggert, J. L. Peterson, N. B. Meezan, S. Le Pape,
1003 G. W. Collins, R. Jeanloz, and R. J. Hemley, *Science* **361**, 677 (2018).

1004 ³⁹M. Schöttler and R. Redmer, *Phys. Rev. Lett.* **120**, 115703 (2018).

1005 ⁴⁰N. Medvedev, H. O. Jeschke, and B. Ziaja, *Physical Review B* **88**, 224304 (2013).

1006 ⁴¹H.-K. Mao and W. Mao, in *Treatise on Geophysics*, edited by G. Schubert (Elsevier,
1007 Amsterdam, 2007) pp. 231 – 267.

1008 ⁴²Z. Jenei, H. P. Liermann, R. Husband, A. S. J. Mndez, D. Pennicard, H. Marquardt,
1009 E. F. O’Bannon, A. Pakhomova, Z. Konôpková, K. Glazyrin, M. Wendt, S. Wenz, E. E.
1010 McBride, W. Morgenroth, B. Winkler, A. Rothkirch, M. Hanfland, and W. J. Evans,
1011 *Review of Scientific Instruments* **90**, 065114 (2019).

1012 ⁴³A. Dewaele, G. Fiquet, and P. Gillet, *Review of Scientific Instruments* **69**, 2421 (1998).

1013 ⁴⁴H. Sinn, HASYLAB Annual Report (2007).

1014 ⁴⁵T. Roth, W. Freund, U. Boesenberg, G. Carini, S. Song, G. Lefevre, A. Goikhman,
1015 M. Fischer, M. Schreck, J. Grunert, and A. Madsen, *Journal of Synchrotron Radiation*
1016 **25**, 177 (2018).

1017 ⁴⁶N. Gomez-Perez, J. F. Rodriguez, and R. S. McWilliams, *Journal of Applied Physics* **121**,
1018 145904 (2017).

1019 ⁴⁷J. S. Loveday, M. I. McMahon, and R. J. Nelmes, *Journal of Applied Crystallography* **23**,
1020 392 (1990).

1021 ⁴⁸R. Jeanloz, P. M. Celliers, G. W. Collins, J. H. Eggert, K. K. M. Lee, R. S. McWilliams,
1022 S. Brygoo, and P. Loubeyre, *Proceedings of the National Academy of Sciences* **104**, 9172
1023 (2007).

1024 ⁴⁹E. S. G. Rainey, J. W. Hernlund, and A. Kavner, *Journal of Applied Physics* **114**, 204905
1025 (2013).

1026 ⁵⁰L. Dubrovinsky, N. Dubrovinskaia, V. B. Prakapenka, and A. M. Abakumov, *Nature*
1027 *Communications* **3**, 1163 (2012).

1028 ⁵¹J. T. Larsen and S. M. Lane, *Journal of Quantitative Spectroscopy and Radiative Transfer*
1029 **51**, 179 (1994).

1030 ⁵²F. Dorchie, V. Recoules, J. Bouchet, C. Fourment, P. M. Leguay, B. I. Cho, K. Engelhorn,
1031 M. Nakatsutsumi, C. Ozkan, T. Tschentscher, M. Harmand, S. Toleikis, M. Störmer,
1032 E. Galtier, H. J. Lee, B. Nagler, P. A. Heimann, and J. Gaudin, *Phys. Rev. B* **92**, 144201
1033 (2015).

1034 ⁵³R. Grover and P. A. Urtiew, *Journal of Applied Physics* **45**, 146 (1974).

1035 ⁵⁴M. H. Seaberg, B. Holladay, J. C. T. Lee, M. Sikorski, A. H. Reid, S. A. Montoya, G. L.
1036 Dakovski, J. D. Koralek, G. Coslovich, S. Moeller, W. F. Schlotter, R. Streubel, S. D.
1037 Kevan, P. Fischer, E. E. Fullerton, J. L. Turner, F.-J. Decker, S. K. Sinha, S. Roy, and
1038 J. J. Turner, *Phys. Rev. Lett.* **119**, 067403 (2017).

1039 ⁵⁵M. O. Wiedorn et. al., *Nature Communications* **9**, 4025 (2018).

1040 ⁵⁶A. Schiffrin, T. Paasch-Colberg, N. Karpowicz, V. Apalkov, D. Gerster, S. Mühlbrandt,
1041 M. Korbman, J. Reichert, M. Schultze, S. Holzner, J. V. Barth, R. Kienberger, R. Ern-
1042 storfer, V. S. Yakovlev, M. I. Stockman, and F. Krausz, *Nature* **493**, 70 (2012).